# Parameter-robust methods for the Biot–Stokes interfacial coupling without Lagrange multipliers

Wietse M. Boon [a,1], Martin Hornkjøl [b], Miroslav Kuchta [c,*,2], Kent-André Mardal [b,c,3], Ricardo Ruiz-Baier [d,e,f,4]

[a] *KTH Royal Institute of Technology, Lindstedtsvägen 25, 114 28, Stockholm, Sweden*
[b] *Department of Mathematics, University of Oslo, Norway*
[c] *Simula Research Laboratory, 0164 Oslo, Norway*
[d] *School of Mathematics, Monash University, 9 Rainforest Walk, Melbourne, 3800 VIC, Australia*
[e] *World-Class Research Center "Digital biodesign and personalized healthcare", Sechenov First Moscow State Medical University, Moscow, Russia*
[f] *Research Core on Natural and Exact Sciences, Universidad Adventista de Chile, Casilla 7-D, Chillán, Chile*

**A R T I C L E   I N F O**

**A B S T R A C T**

In this paper we advance the analysis of discretizations for a fluid-structure interaction model of the monolithic coupling between the free flow of a viscous Newtonian fluid and a deformable porous medium separated by an interface. A five-field mixed-primal finite element scheme is proposed solving for Stokes velocity-pressure and Biot displacement-total pressure-fluid pressure. Adequate inf-sup conditions are derived, and one of the distinctive features of the formulation is that its stability is established robustly in all material parameters. We propose robust preconditioners for this perturbed saddle-point problem using appropriately weighted operators in fractional Sobolev and metric spaces at the interface. The performance is corroborated by several test cases, including the application to interfacial flow in the brain.

© 2022 Elsevier Inc. All rights reserved.

## 1. Introduction

### 1.1. Scope

We address the construction of appropriate monolithic solvers for multiphysics fluid-poromechanical couplings interacting through an interface. Particular attention is payed to tracking parameter dependence of the continuous and discrete formulations so that the resulting numerical methods are robust with respect to typical scales in material constants span-

---

ning over many orders of magnitude. We adopt a multi-domain approach, where appropriate conditions for the coupling through the shared interface need to be imposed. We use the conditions proposed in [1] (although, other forms and dedicated phenomena could be incorporated without much effort, such as fluid entry resistance [2,3]). The recent literature contains various numerical methods for (Navier–)Stokes/Biot interface formulations including mixed, double mixed, monolithic, segregated, conforming, non-conforming, and DG discretizations [4–15].

In [12,16] (and starting from the Biot–Stokes equations advanced in [5,17]) the authors rewrite the poroelasticity equations using displacement, fluid pressure and total pressure (also as in the poromechanics formulations from [18–20]). Since fluid pressure in the poroelastic domain has sufficient regularity, no Lagrange multipliers are needed to enforce the coupling conditions, which resembles the different formulations for Stokes-Darcy advanced in [21–24]. Another advantage of the three-field Biot formulation is its robustness with respect to the Lamé constants of the poroelastic structure. This robustness is of particular importance when we test the flow response to changes in the material properties of the skeleton and when the solid is nearly incompressible. The work [12] focuses on the stability analysis and its precise implications on the asymptotics of the interface conditions when the permeability depends on porosity heterogeneity, whereas [16] addresses the stability of the semi- and fully discrete problems, and the application to interfacial flow in the eye. Here, we extend these works by concentrating on deriving robust stability, on designing efficient block preconditioners (robust with respect to all material parameters) following the general theoretical formalism from [25], and on the simulation of free flow interacting with interstitial flow in the brain. In such a context (and in the wider class of problems we consider in this paper), tissue permeability is of the order of $10^{-15}$ m$^2$, and the incorporation of tangential interface transmission conditions usually involves terms that scale inversely proportional to the square root of permeability. Moreover, the solid is nearly incompressible, making the first Lamé parameter significantly larger than the other mechanical parameters and exhibiting volumetric locking for some types of displacement-based formulations. Other flow regimes that are challenging include low-storage cases [26]. It is then important that the stability and convergence of the numerical approximations are preserved within the parameter ranges of interest.

Here we follow [27,28,20,29] and use parameter-weighted norms to achieve robustness. However, as we will see, combining proper preconditioners for Stokes and Biot single-physics problems is not sufficient for the interface coupled problem. In fact, the condition number of the preconditioned system, although robust in mesh size, grows like the square root of the ratio between fluid viscosity and permeability. This phenomenon is demonstrated in Example 2.1, below. That is, the efficiency of seemingly natural preconditioners varies with the material parameters. In order to regain stability with respect to all parameters, we include both an additional fractional term involving the pressure and a metric term coupling the tangential fluid velocity and solid displacement at the interface, hereby increasing the regularity at the interface in a proper parameter dependent manner. This strategy draws inspiration from similar approaches employed in the design of robust solvers for Darcy and Stokes-Darcy couplings [30,21,23].

### 1.2. Outline

We have organised the contents of this paper in the following manner. The remainder of this section contains preliminaries on notation and functional spaces to be used throughout the manuscript. Section 2 outlines the main details of the balance equations, stating typical interfacial and boundary conditions, and restricting the discussion to the steady Biot–Stokes coupled problem. There we also include the weak formulation and demonstrate that simple diagonal preconditioners based on standard norms do not lead to robustness over the whole parameter range. This issue is addressed in Section 3 where we show well-posedness of the system using a global inf-sup argument with parameter weighted operators in fractional spaces, which in turn assist in the design of robust solvers by operator preconditioning. Section 4 discusses finite element discretization of the coupled problem using both conforming and non-conforming elements; and it also contains numerical experiments demonstrating robustness of the fractional preconditioner and its feasibility for simplified simulations of interfacial flow in the brain.

### 1.3. Preliminaries

Let us consider a spatial domain $\Omega \subset \mathbb{R}^d$, where $d = 2, 3$, disjointly split into $\Omega_F$ and $\Omega_P$. These subdomains respectively represent the region filled with an incompressible fluid and the elastic porous medium (a deformable solid matrix or an array of solid particles). We will denote by $\boldsymbol{n}$ the unit normal vector on the boundary $\partial\Omega$, and by $\Sigma = \partial\Omega_F \cap \partial\Omega_P$ the interface between the two subdomains, which is assumed sufficiently regular. We adopt the convention that on $\Sigma$ the normal vector points from $\Omega_F$ to $\Omega_P$. We also define the boundaries $\Gamma_F = \partial\Omega_F \setminus \Sigma$ and $\Gamma_P = \partial\Omega_P \setminus \Sigma$. The sub-boundary $\Gamma_F$ is further decomposed between $\Gamma_F^{\boldsymbol{u}}$ and $\Gamma_F^{\boldsymbol{\sigma}}$ where we impose, respectively, no slip velocities and zero normal total stresses. Similarly, we split $\Gamma_P$ into $\Gamma_P^{p_P}$ and $\Gamma_P^{\boldsymbol{d}}$ where we prescribe zero traction and clamped boundaries, respectively. For the analysis, the setup of trace spaces needs that $\mathrm{dist}(\Sigma, \Gamma_P^{p_P}) > 0$ and that $\mathrm{dist}(\Sigma, \Gamma_F^{\boldsymbol{\sigma}}) > 0$, which can be satisfied if the interface meets the boundary at the Biot displacement and Stokes velocity boundaries (see Fig. 1.1, left), where $\Gamma_P^{\boldsymbol{d}} = \Gamma_{1,P}^{\boldsymbol{d}} \cup \Gamma_{2,P}^{\boldsymbol{d}}$ and $\Gamma_F^{\boldsymbol{u}} = \Gamma_{1,F}^{\boldsymbol{u}} \cup \Gamma_{2,F}^{\boldsymbol{u}}$. Our numerical tests will also include cases where the interface intersects boundaries $\Gamma_F^{\boldsymbol{\sigma}}$ and $\Gamma_P^{p_P}$ on the Stokes and Biot sides, respectively.
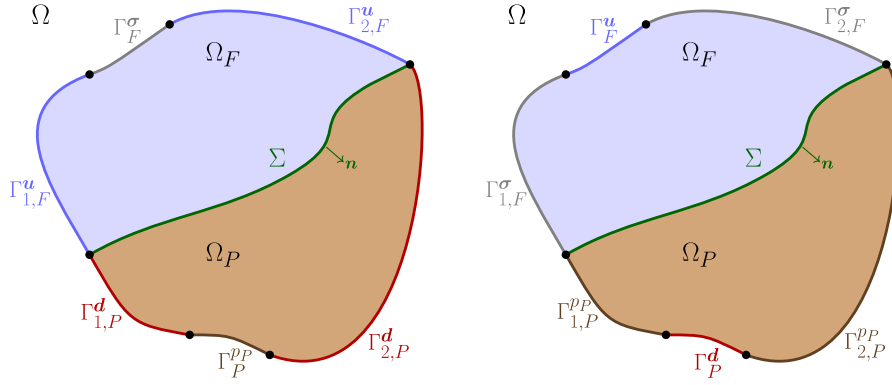
**Fig. 1.1.** A configuration of subdomains and boundary partition for the Biot–Stokes coupled problem. (Left) Setup assumed for the analysis in Theorem 3.1. (Right) Example of another configuration investigated by some of the numerical experiments in Section 4.4.

For a normed space $X$ and a scalar $\zeta > 0$, the weighted space $\zeta X$ refers to $X$ endowed with the norm $\zeta \| \cdot \|_X$. Moreover, if $X, Y$ are Hilbert spaces, then the intersection $X \cap Y$ provided with the norm $\|v\|_{X \cap Y}^2 = \|v\|_X^2 + \|v\|_Y^2$, is also a Hilbert space [30,31].

Vector fields and vector-valued spaces will be written in boldface. In addition, by $L^2(\Omega)$ we will denote the usual Lebesgue space of square integrable functions and $H^m(\Omega)$ denotes the usual Sobolev space with weak derivatives of order up to $m$ in $L^2(\Omega)$, and $\mathbf{H}^m(\Omega)$ denotes its vector counterpart. In addition, $\mathbf{L}_{\mathbf{t}}^2(\Sigma)$ will denote the space of functions $\mathbf{z} : \Omega_i \to \mathbb{R}^d$, $i \in \{F, P\}$, such that $\mathbf{z} - \mathbf{n}(\mathbf{z} \cdot \mathbf{n}) \in \mathbf{L}^2(\Sigma)$.

An $L^2(\Omega)$ (as well as $\mathbf{L}^2(\Omega)$) inner product over a generic bounded domain $\Omega$ is denoted as $(\cdot, \cdot)_\Omega$. The symbol $\langle \cdot, \cdot \rangle_\Sigma$ will denote the pairing between the trace functional space $H^{1/2}(\Sigma)$ and its dual $H^{-1/2}(\Sigma)$, and we will also write $\langle \cdot, \cdot \rangle$ to denote other, more general, duality pairings. Moreover, for $\mathbf{z} \in \mathbf{H}^1(\Omega_i) \cap \mathbf{L}_{\mathbf{t}}^2(\Sigma)$, its normal and tangential traces defined by bounded surjective maps, will be denoted by $T_{\mathbf{n}} \mathbf{z} \in H^{1/2}(\Sigma)$ and $T_{\mathbf{t}} \mathbf{z} \in \mathbf{L}^2(\Sigma)$, respectively [23]. We also remark that, while $H^{1/2}(\Sigma)$ is a subspace of $L^2(\Sigma)$ as a set, the tangential trace of $\mathbf{z} \in \zeta_1 \mathbf{H}^1(\Omega_i) \cap \zeta_2 \mathbf{L}_{\mathbf{t}}^2(\Sigma)$ is in $\zeta_1 \mathbf{H}^{1/2}(\Sigma) \cap \zeta_2 \mathbf{L}^2(\Sigma)$ and that in our setting it is important to track the parameter dependence for the sake of robustness.

Pertaining to the poroelastic domain, and assuming momentarily that $|\Gamma_P^{\mathbf{d}}| = 0$, we recall from [32, Section 2.4.2] the definition of the space

$$H_{00}^{1/2}(\Sigma) = \{\eta \in H^{1/2}(\Sigma) : E_{00}(\eta) \in H^{1/2}(\partial \Omega_P)\}, \tag{1.1}$$

supplied with the norm

$$\|\eta\|_{1/2,00,\Sigma} := \|E_{00}(\eta)\|_{1/2,\partial \Omega_P},$$

where $E_{00} : H^{1/2}(\Sigma) \to H^{1/2}(\partial \Omega_P)$ denotes the extension-by-zero operator

$$E_{00}(\eta) = \begin{cases} \eta & \text{on } \Sigma, \\ 0 & \text{on } \partial \Omega_P \setminus \Sigma, \end{cases} \quad \forall \eta \in H^{1/2}(\Sigma).$$

Furthermore, the restriction of $\psi \in H^{-1/2}(\partial \Omega_P)$ to $\Sigma$, defined as

$$\langle \psi|_\Sigma, \eta \rangle_\Sigma = \langle \psi, E_{00}(\eta) \rangle_{\partial \Omega_P} \quad \forall \eta \in H_{00}^{1/2}(\Sigma),$$

belongs to the dual $[H_{00}^{1/2}(\Sigma)]'$ of $H_{00}^{1/2}(\Sigma)$. Its norm is

$$\|\psi|_\Sigma\|_{-1/2,00,\Sigma} := \sup_{0 \neq \eta \in H_{00}^{1/2}(\Sigma)} \frac{\langle \psi|_\Sigma, \eta \rangle_\Sigma}{\|\eta\|_{1/2,00,\Sigma}} = \sup_{0 \neq \eta \in H_{00}^{1/2}(\Sigma)} \frac{\langle \psi, E_{00}(\eta) \rangle_{\partial \Omega_P}}{\|E_{00}(\eta)\|_{1/2,\partial \Omega_P}}. \tag{1.2}$$

The boundary setup in Fig. 1.1 is such that $|\Gamma_P^{\mathbf{d}}| \cdot |\Gamma_P^{p_P}| > 0$, and therefore a modification of (1.1)-(1.2) is required. With that purpose, we note that any $\eta \in H^{1/2}(\Sigma)$ can be continuously extended to $\varphi$ in the space

$$H_{01}^{1/2}(\Sigma) := \{\eta \in H^{1/2}(\Sigma) : E_{01}(\eta) \in H^{1/2}(\Gamma_1)\}, \tag{1.3}$$

where $\bar{\Gamma}_1 := \bar{\Sigma} \cup \bar{\Gamma}_{1,P}^{\mathbf{d}} \cup \bar{\Gamma}_{2,P}^{\mathbf{d}}$ (see Fig. 1.1, left), and

$$E_{01}(\eta) = \begin{cases} \eta & \text{on } \Sigma, \\ 0 & \text{on } \Gamma_P^{\mathbf{d}}, \end{cases} \quad \forall \eta \in H^{1/2}(\Sigma).$$

This treatment can be interpreted as replacing $H_{00}^{1/2}(\Sigma)$ by the space of functions $\eta \in H^{1/2}(\Sigma)$ such that $\xi^{-1/2}\eta \in L^2(\Sigma)$, where $\xi$ is a sufficiently regular trace function, positive on $\Sigma$, and vanishing only on $\Gamma_P^{\boldsymbol{d}}$ (see, for example, [33]).

The norm of the resulting extension $\varphi \in H_{01}^{1/2}(\Sigma)$ is defined analogously as before,

$$\|\varphi\|_{1/2,01,\Sigma} := \|E_{01}(\varphi)\|_{1/2,\Gamma_1}, \tag{1.4}$$

and therefore the restriction of a distribution to the interface, $\psi|_\Sigma$, is in the dual space $[H_{01}^{1/2}(\Sigma)]'$ and its norm is

$$\|\psi|_\Sigma\|_{-1/2,01,\Sigma} := \sup_{0 \neq \eta \in H_{01}^{1/2}(\Sigma)} \frac{\langle \psi|_\Sigma, \eta \rangle_\Sigma}{\|\eta\|_{1/2,01,\Sigma}} = \sup_{0 \neq \eta \in H_{01}^{1/2}(\Sigma)} \frac{\langle \psi, E_{01}(\eta) \rangle_{\Gamma_1}}{\|E_{01}(\eta)\|_{1/2,\Gamma_1}}. \tag{1.5}$$

Finally, we consider a problem: Given $\mathcal{A} : X \to X'$, $b \in X'$ find $x \in X$ satisfying $\mathcal{A}x = b$ in $X'$. From the continuous perspective [25,34], the problem can be solved iteratively by Krylov methods, however, the operator involved is required to map the space $X$ to itself. We shall therefore consider a preconditioner $\mathcal{R} : X' \to X$ and apply Krylov methods to the (left-) preconditioned problem $\mathcal{R}\mathcal{A}x = \mathcal{R}b$. The Biot-Stokes problem considered further will yield symmetric saddle point system and we will therefore consider the Minimal Residual (MinRes) method.[5] Moreover, the left preconditioned MinRes method has a sharp and well developed theory for indefinite symmetric problems, see the seminal papers [36,37]. In particular, the method's convergence is determined by the spectrum of the generalized eigenvalue problem

$$\mathcal{A}u_i = \lambda_i \mathcal{R}^{-1} u_i,$$

and the convergence rate (of the residual measured in the norm induced by $\mathcal{R}^{-1}$) can be estimated in terms of the spectral condition number $\max_i |\lambda_i| / \min_i |\lambda_i|$, see [38,34].

## 2. Governing equations and weak formulation

The momentum and mass balance equations for the flow in the fluid cavity are given by Stokes equations written in terms of fluid velocity $\boldsymbol{u}$ and fluid pressure $p_F$, whereas the non-viscous filtration flow through the porous skeleton can be described by Darcy's law in terms of pressure head $p_P$, and the porous matrix elastostatics are stated in terms of the solid displacement $\boldsymbol{d}$. The coupled Biot–Stokes equations arising after a backward Euler semi-discretization in time, with time step $\Delta t$, read

$$-\mathbf{div}[2\mu_f \boldsymbol{\epsilon}(\boldsymbol{u}) - p_F \mathbf{I}] = \rho_f \boldsymbol{g} \qquad \text{in } \Omega_F, \tag{2.1a}$$

$$\text{div}\, \boldsymbol{u} = 0 \qquad \text{in } \Omega_F, \tag{2.1b}$$

$$-\mathbf{div}[2\mu_s \boldsymbol{\epsilon}(\boldsymbol{d}) - \varphi \mathbf{I}] = \rho_s \boldsymbol{f} \qquad \text{in } \Omega_P, \tag{2.1c}$$

$$\varphi - \alpha p_P + \lambda \, \text{div}\, \boldsymbol{d} = 0 \qquad \text{in } \Omega_P, \tag{2.1d}$$

$$\left(C_0 + \frac{\alpha^2}{\lambda}\right)\frac{1}{\Delta t}p_P - \frac{\alpha}{(\Delta t)\lambda}\varphi - \text{div}\left(\frac{\kappa}{\mu_f}\nabla p_P - \rho_f \boldsymbol{g}\right) = m_P \qquad \text{in } \Omega_P, \tag{2.1e}$$

where $\boldsymbol{f}$ is a vector field of body loads, $\boldsymbol{g}$ is the gravity acceleration, $\mu_f$ is the fluid viscosity, $\boldsymbol{\epsilon}(\boldsymbol{u}) = \frac{1}{2}(\nabla \boldsymbol{u} + \nabla \boldsymbol{u}^{\mathrm{t}})$ is the strain rate tensor, and $\boldsymbol{\epsilon}(\boldsymbol{d}) = \frac{1}{2}(\nabla \boldsymbol{d} + \nabla \boldsymbol{d}^{\mathrm{t}})$ is the infinitesimal strain tensor, $\rho_f, \rho_s$ are the density of the fluid and solid, respectively, $\lambda, \mu_s$ are the first and second Lamé constants of the solid, $\kappa$ is the heterogeneous tensor of permeabilities (satisfying $|\boldsymbol{w}|^2 \lesssim \boldsymbol{w} \cdot \kappa(\boldsymbol{x})\boldsymbol{w}$ a.e. in $\Omega_P$ and for all $\boldsymbol{w} \in \mathbb{R}^d$); $m_P$ is a source/sink term for the fluid pressure (which also includes pressures in the previous backward Euler time step); and $C_0, \alpha$ are the total storage capacity and Biot–Willis poroelastic coefficient. Here we have used the total pressure $\varphi := \alpha p_P - \lambda \, \text{div}\, \boldsymbol{d}$, as an additional unknown [27,20].

We furthermore supply boundary conditions as follows

$$\boldsymbol{u} = \boldsymbol{0} \qquad \text{on } \Gamma_F^{\boldsymbol{u}}, \tag{2.2a}$$

$$[2\mu_f \boldsymbol{\epsilon}(\boldsymbol{u}) - p_F \mathbf{I}]\boldsymbol{n} = \boldsymbol{0} \qquad \text{on } \Gamma_F^{\boldsymbol{\sigma}}, \tag{2.2b}$$

$$\boldsymbol{d} = \boldsymbol{0} \quad \text{and} \quad \frac{\kappa}{\mu_f}\nabla p_P \cdot \boldsymbol{n} = 0 \qquad \text{on } \Gamma_P^{\boldsymbol{d}}, \tag{2.2c}$$

$$[2\mu_s \boldsymbol{\epsilon}(\boldsymbol{d}) - \varphi \mathbf{I}]\boldsymbol{n} = \boldsymbol{0} \quad \text{and} \quad p_P = p_0 \qquad \text{on } \Gamma_P^{p_P}. \tag{2.2d}$$

---

[5] The MinRes algorithm utilizes a short three term recurrence and is thus more memory efficient than, e.g., the Generalized Minimal Residual (GMRes) method. However, due to accumulation of errors in floating point arithmetic the required orthogonality might be lost leading to slower convergence of MinRes compared to GMRes which employs (full/partial) reorthogonalization [35].

In order to close the system, we consider the classical transmission conditions on $\Sigma$ accounting for the continuity of normal fluxes, momentum balance, equilibrium of fluid normal stresses, and the so-called Beavers–Joseph–Saffman condition for tangential fluid forces [7,2], which in the present setting reduce to

$$\boldsymbol{u} \cdot \boldsymbol{n} = (\frac{1}{\Delta t}\boldsymbol{d} - \frac{\kappa}{\mu_f}\nabla p_P) \cdot \boldsymbol{n} \qquad\qquad \text{on } \Sigma, \tag{2.3a}$$

$$(2\mu_f\boldsymbol{\epsilon}(\boldsymbol{u}) - p_F\mathbf{I})\boldsymbol{n} = (2\mu_s\boldsymbol{\epsilon}(\boldsymbol{d}) - \varphi\mathbf{I})\boldsymbol{n} \qquad\qquad \text{on } \Sigma, \tag{2.3b}$$

$$-\boldsymbol{n} \cdot (2\mu_f\boldsymbol{\epsilon}(\boldsymbol{u}) - p_F\mathbf{I})\boldsymbol{n} = p_P \qquad\qquad \text{on } \Sigma, \tag{2.3c}$$

$$-\boldsymbol{n} \cdot (2\mu_f\boldsymbol{\epsilon}(\boldsymbol{u}) - p_F\mathbf{I})\boldsymbol{t}_j = \frac{\gamma\mu_f}{\sqrt{\kappa}}(\boldsymbol{u} - \frac{1}{\Delta t}\boldsymbol{d}) \cdot \boldsymbol{t}_j, \quad 1 \le j \le d-1 \qquad \text{on } \Sigma, \tag{2.3d}$$

where $\gamma > 0$ is the slip rate coefficient depending on the geometry of the domain, and we recall that the normal $\boldsymbol{n}$ on the interface is understood as pointing from the fluid domain $\Omega_F$ towards the porous structure $\Omega_P$, while $\boldsymbol{t}_j$, $1 \le j \le d-1$ are orthonormal tangent vectors on $\Sigma$, normal to $\boldsymbol{n}$.

The challenging model parameters are $\mu_f$, $C_0$, $\lambda$, $\gamma$, $\alpha$, and the magnitude of $\kappa$. Therefore, we will concentrate on the specific case where $\Delta t = 1$, and the model parameters (in particular $\kappa$) are spatially constant. Owing to the specification of boundary conditions (2.2), we define the following Hilbert spaces

$$\mathbf{H}^1_\star(\Omega_F) = \{\boldsymbol{v} \in \mathbf{H}^1(\Omega_F) : \boldsymbol{v}|_{\Gamma^{\boldsymbol{u}}_F} = \mathbf{0}\}, \quad \mathbf{H}^1_\star(\Omega_P) = \{\boldsymbol{w} \in \mathbf{H}^1(\Omega_P) : \boldsymbol{w}|_{\Gamma^{\boldsymbol{d}}_P} = \mathbf{0}\},$$

$$H^1_\star(\Omega_P) = \{q_P \in H^1(\Omega_P) : q_P|_{\Gamma^{p_P}_P} = 0\}. \tag{2.4}$$

We then proceed to test (2.1a)-(2.1e) against suitable smooth functions and to integrate over the corresponding subdomain, to arrive at

$$2\mu_f(\boldsymbol{\epsilon}(\boldsymbol{u}), \boldsymbol{\epsilon}(\boldsymbol{v}))_{\Omega_F} - (p_F, \operatorname{div}\boldsymbol{v})_{\Omega_F} - \langle(2\mu_f\boldsymbol{\epsilon}(\boldsymbol{u}) - p_F\mathbf{I})\boldsymbol{n}, \boldsymbol{v}\rangle_\Sigma = F^F(\boldsymbol{v}) \qquad \forall \boldsymbol{v} \in \mathbf{H}^1_\star(\Omega_F),$$

$$2\mu_s(\boldsymbol{\epsilon}(\boldsymbol{d}), \boldsymbol{\epsilon}(\boldsymbol{w}))_{\Omega_P} - (\varphi, \operatorname{div}\boldsymbol{w})_{\Omega_P} + \langle(2\mu_s\boldsymbol{\epsilon}(\boldsymbol{d}) - \varphi\mathbf{I})\boldsymbol{n}, \boldsymbol{w}\rangle_\Sigma = F^P(\boldsymbol{w}) \qquad \forall \boldsymbol{w} \in \mathbf{H}^1_\star(\Omega_P),$$

$$-(\operatorname{div}\boldsymbol{u}, q_F)_{\Omega_F} = 0 \qquad \forall q_F \in L^2(\Omega_F),$$

$$\frac{1}{\lambda}(\alpha p_P - \varphi, \psi)_{\Omega_P} - (\operatorname{div}\boldsymbol{d}, \psi)_{\Omega_P} = 0 \qquad \forall \psi \in L^2(\Omega_P),$$

$$-\big(C_0 + \frac{\alpha^2}{\lambda}\big)(p_P, q_P)_{\Omega_P} + \frac{\alpha}{\lambda}(q_P, \varphi)_{\Omega_P} - \frac{\kappa}{\mu_f}(\nabla q_P, \nabla p_P)_{\Omega_P} + \langle\frac{\kappa}{\mu_f}\nabla p_P \cdot \boldsymbol{n}, q_P\rangle_\Sigma = G(q_P) \qquad \forall q_P \in H^1_\star(\Omega_P),$$

where

$$F^F(\boldsymbol{v}) = \rho_f(\boldsymbol{g}, \boldsymbol{v})_{\Omega_F}, \quad F^P(\boldsymbol{w}) = \rho_s(\boldsymbol{f}, \boldsymbol{w})_{\Omega_P}, \quad G(q_P) = -(m_P, q_P)_{\Omega_P} - \rho_f(\boldsymbol{g}, \nabla q_P)_{\Omega_P} + \rho_f\langle\boldsymbol{g} \cdot \boldsymbol{n}, q_P\rangle_\Sigma.$$

The interfacial term in the Stokes momentum balance satisfies

$$-\langle(2\mu_f\boldsymbol{\epsilon}(\boldsymbol{u}) - p_F\mathbf{I})\boldsymbol{n}, \boldsymbol{v}\rangle_\Sigma = -\langle T_{\boldsymbol{n}}[(2\mu_f\boldsymbol{\epsilon}(\boldsymbol{u}) - p_F\mathbf{I})\boldsymbol{n}], T_{\boldsymbol{n}}\boldsymbol{v}\rangle_\Sigma - \langle T_{\boldsymbol{t}}[(2\mu_f\boldsymbol{\epsilon}(\boldsymbol{u}) - p_F\mathbf{I})\boldsymbol{n}], T_{\boldsymbol{t}}\boldsymbol{v}\rangle_\Sigma$$

$$= \langle p_P, T_{\boldsymbol{n}}\boldsymbol{v}\rangle_\Sigma + \frac{\gamma\mu_f}{\sqrt{\kappa}}\langle T_{\boldsymbol{t}}(\boldsymbol{u} - \boldsymbol{d}), T_{\boldsymbol{t}}\boldsymbol{v}\rangle_\Sigma, \tag{2.5}$$

where in the last line we have used the interface conditions (2.3c) and (2.3d). In turn, for the interfacial term in the Biot momentum balance we get

$$\langle(2\mu_s\boldsymbol{\epsilon}(\boldsymbol{d}) - \varphi\mathbf{I})\boldsymbol{n}, \boldsymbol{w}\rangle_\Sigma = \langle(2\mu_f\boldsymbol{\epsilon}(\boldsymbol{u}) - p_F\mathbf{I})\boldsymbol{n}, \boldsymbol{w}\rangle_\Sigma$$

$$= -\langle p_P, T_{\boldsymbol{n}}\boldsymbol{w}\rangle_\Sigma - \frac{\gamma\mu_f}{\sqrt{\kappa}}\langle T_{\boldsymbol{t}}(\boldsymbol{u} - \boldsymbol{d}), T_{\boldsymbol{t}}\boldsymbol{w}\rangle_\Sigma, \tag{2.6}$$

where the first equality comes from the transmission condition (2.3b), and the second one from (2.5). Similarly, for the interfacial term in the Biot mass conservation equation we use the continuity condition (2.3a). Combining such a relation with (2.5)-(2.6), we readily arrive at the following remainder on the interface

$$\langle p_P, T_{\boldsymbol{n}}(\boldsymbol{v} - \boldsymbol{w})\rangle_\Sigma + \frac{\gamma\mu_f}{\sqrt{\kappa}}\langle T_{\boldsymbol{t}}(\boldsymbol{u} - \boldsymbol{d}), T_{\boldsymbol{t}}(\boldsymbol{v} - \boldsymbol{w})\rangle_\Sigma + \langle T_{\boldsymbol{n}}(\boldsymbol{u} - \boldsymbol{d}), q_P\rangle_\Sigma. \tag{2.7}$$

The functional spaces (2.4) provide sufficient regularity for all the terms in the expression (2.7) to be well-defined (implying in particular that, differently from e.g. Stokes–Darcy problems in mixed form, no additional Lagrange multipliers are required to realize the coupling conditions). We also define the product space $\mathbf{H}$

$$\mathbf{H} = \mathbf{H}^1_\star(\Omega_F) \times \mathbf{H}^1_\star(\Omega_P) \times L^2(\Omega_F) \times L^2(\Omega_P) \times H^1_\star(\Omega_P), \tag{2.8}$$

and, using (2.7), proceed to rearrange the weak form above to have: Find $(\boldsymbol{u}, \boldsymbol{d}, p_F, \varphi, p_P) \in \mathbf{H}$ such that

$$2\mu_f(\boldsymbol{\epsilon}(\boldsymbol{u}), \boldsymbol{\epsilon}(\boldsymbol{v}))_{\Omega_F} + \frac{\gamma \mu_f}{\sqrt{\kappa}} \langle T_{\boldsymbol{t}}(\boldsymbol{u} - \boldsymbol{d}), T_{\boldsymbol{t}} \boldsymbol{v}\rangle_\Sigma$$
$$-(p_F, \operatorname{div} \boldsymbol{v})_{\Omega_F} + \langle p_P, T_{\boldsymbol{n}} \boldsymbol{v}\rangle_\Sigma = F^F(\boldsymbol{v}) \qquad \forall \boldsymbol{v} \in \mathbf{H}^1_\star(\Omega_F), \tag{2.9a}$$

$$\frac{\gamma \mu_f}{\sqrt{\kappa}} \langle T_{\boldsymbol{t}}(\boldsymbol{d} - \boldsymbol{u}), T_{\boldsymbol{t}} \boldsymbol{w}\rangle_\Sigma + 2\mu_s(\boldsymbol{\epsilon}(\boldsymbol{d}), \boldsymbol{\epsilon}(\boldsymbol{w}))_{\Omega_P}$$
$$-(\varphi, \operatorname{div} \boldsymbol{w})_{\Omega_P} - \langle p_P, T_{\boldsymbol{n}} \boldsymbol{w}\rangle_\Sigma = F^P(\boldsymbol{w}) \qquad \forall \boldsymbol{w} \in \mathbf{H}^1_\star(\Omega_P), \tag{2.9b}$$

$$-(\operatorname{div} \boldsymbol{u}, q_F)_{\Omega_F} = 0 \qquad \forall q_F \in L^2(\Omega_F), \tag{2.9c}$$

$$\frac{1}{\lambda}(\alpha p_P - \varphi, \psi)_{\Omega_P} - (\operatorname{div} \boldsymbol{d}, \psi)_{\Omega_P} = 0 \qquad \forall \psi \in L^2(\Omega_P), \tag{2.9d}$$

$$-\Big(C_0 + \frac{\alpha^2}{\lambda}\Big)(p_P, q_P)_{\Omega_P} + \frac{\alpha}{\lambda}(q_P, \varphi)_{\Omega_P}$$
$$+\langle q_P, T_{\boldsymbol{n}}(\boldsymbol{u} - \boldsymbol{d})\rangle_\Sigma - \frac{\kappa}{\mu_f}(\nabla q_P, \nabla p_P)_{\Omega_P} = G(q_P) \qquad \forall q_P \in H^1_\star(\Omega_P). \tag{2.9e}$$

System (2.9) differs from that analyzed in [16] in the ordering of the unknowns, and in that we obtain a symmetric multilinear formulation defined by a global operator $\mathcal{A}$ (the coefficient matrix of the left-hand side of (2.9)) of the form

$$\begin{pmatrix} -2\mu_f \operatorname{\mathbf{div}} \boldsymbol{\epsilon} + \frac{\gamma \mu_f}{\sqrt{\kappa}} T'_{\boldsymbol{t}} T_{\boldsymbol{t}} & -\frac{\gamma \mu_f}{\sqrt{\kappa}} T'_{\boldsymbol{t}} & \nabla & & T'_{\boldsymbol{n}} \\ -\frac{\gamma \mu_f}{\sqrt{\kappa}} T_{\boldsymbol{t}} & -2\mu_s \operatorname{\mathbf{div}} \boldsymbol{\epsilon} + \frac{\gamma \mu_f}{\sqrt{\kappa}} T'_{\boldsymbol{t}} T_{\boldsymbol{t}} & \nabla & & -T'_{\boldsymbol{n}} \\ \hdashline -\operatorname{div} & & & & \\ & -\operatorname{div} & -\frac{1}{\lambda} I & \frac{\alpha}{\lambda} I \\ T_{\boldsymbol{n}} & -T_{\boldsymbol{n}} & \frac{\alpha}{\lambda} I & -\big(C_0 + \frac{\alpha^2}{\lambda}\big)I + \frac{\kappa}{\mu_f} \Delta \end{pmatrix}, \tag{2.10}$$

where the dependence on the model parameters is clearly identified. In particular, the interface coupling terms on the first off-diagonal blocks depend on the inverse of permeability.

We note that $\mathcal{A}$ can be regarded as defining a perturbed saddle-point problem, with

$$\mathcal{A} = \begin{pmatrix} A & B' \\ B & -C \end{pmatrix}, \tag{2.11}$$

where the composing blocks $A : V \to V'$, $B : V \to Q'$, $C : Q \to Q'$ on the spaces

$$V = \mathbf{H}^1_\star(\Omega_F) \times \mathbf{H}^1_\star(\Omega_P), \quad Q = L^2(\Omega_F) \times L^2(\Omega_P) \times H^1_\star(\Omega_P) \tag{2.12}$$

are defined as

$$A = \begin{pmatrix} \mathcal{A}_{FF} & \mathcal{A}_{FP} \\ \mathcal{A}_{PF} & \mathcal{A}_{PP} \end{pmatrix} = \begin{pmatrix} -2\mu_f \operatorname{\mathbf{div}} \boldsymbol{\epsilon} & 0 \\ 0 & -2\mu_s \operatorname{\mathbf{div}} \boldsymbol{\epsilon} \end{pmatrix} + \gamma \frac{\mu_f}{\sqrt{\kappa}} \begin{pmatrix} T'_{\boldsymbol{t}} \\ -T'_{\boldsymbol{t}} \end{pmatrix} \begin{pmatrix} T_{\boldsymbol{t}} & -T_{\boldsymbol{t}} \end{pmatrix}, \tag{2.13a}$$

$$B = \begin{pmatrix} -\operatorname{div} & 0 \\ 0 & -\operatorname{div} \\ T_{\boldsymbol{n}} & -T_{\boldsymbol{n}} \end{pmatrix}, \quad C = \begin{pmatrix} 0 & 0 & 0 \\ 0 & \frac{1}{\lambda} I & -\frac{\alpha}{\lambda} I \\ 0 & -\frac{\alpha}{\lambda} I & \big(C_0 + \frac{\alpha^2}{\lambda}\big)I - \frac{\kappa}{\mu_f} \Delta \end{pmatrix}. \tag{2.13b}$$

In turn, well-posedness of the Biot–Stokes system (2.9) in the product space (2.8) can be established using the abstract Brezzi–Braess theory [39], after invoking separately the solvability and stability results for the Stokes subproblem [40] and the Biot subproblem in the three-field total pressure formulation [27]. However, such a decoupled approach does not lead to stability independent of the material parameters and consequently, preconditioners based on the standard norms (also referred to as single-physics or sub-physics preconditioners) are not necessarily parameter robust. This issue is demonstrated next in Example 2.1.

**Example 2.1** *(Simple preconditioners using standard norms).* We consider the Biot–Stokes formulation (2.9) defined on the subdomains $\Omega_F = (0, \frac{1}{2}) \times (0, 1)$, $\Omega_P = (\frac{1}{2}, 1) \times (0, 1)$ with boundary conditions such that the left edge of $\Omega_F$ is a no-slip boundary $\Gamma^{\boldsymbol{u}}_F$ while the top and bottom edges will form $\Gamma^{\boldsymbol{\sigma}}_F$. Similarly, the top and bottom edges on the Biot side are considered stress-free while the right edge is clamped.

Based on the well-posedness of (2.9) in the space $\mathbf{H}$ (cf. (2.8)), we can readily consider a solution space with weighted inner product leading to the Riesz map (diagonal) preconditioner

**Table 2.1**

Performance of preconditioners (2.14) and (2.15) for the Biot–Stokes system (2.9) in Example 2.1 with different mesh resolutions ($h$). Only the parameters $\mu_f$ and $\kappa$ are varied away from 1. The problem is discretized by TH$_1$ elements, see Appendix A. The lack of convergence after 750 MinRes iterations is indicated as –. The solver is started from a random initial vector and terminates once the preconditioned residual norm is decreased by factor $10^8$.

| | | Preconditioner (2.14) | | | | Preconditioner (2.15) | | | |
|---|---|---|---|---|---|---|---|---|---|
| $\mu_f$ | $\kappa$ ⟍ $h$ | $2^{-2}$ | $2^{-3}$ | $2^{-4}$ | $2^{-5}$ | $2^{-2}$ | $2^{-3}$ | $2^{-4}$ | $2^{-5}$ |
| 1 | $10^{-4}$ | 211 | 240 | 258 | 264 | 71 | 82 | 89 | 89 |
| | $10^{-2}$ | 76 | 76 | 74 | 73 | 50 | 49 | 48 | 48 |
| | 1 | 41 | 41 | 41 | 41 | 37 | 37 | 36 | 36 |
| $\kappa$ | $\mu_f$ ⟍ $h$ | $2^{-2}$ | $2^{-3}$ | $2^{-4}$ | $2^{-5}$ | $2^{-2}$ | $2^{-3}$ | $2^{-4}$ | $2^{-5}$ |
| 1 | $10^{-8}$ | 394 | 184 | – | – | 693 | 471 | 639 | – |
| | $10^{-2}$ | 59 | 59 | 59 | 58 | 58 | 57 | 55 | 55 |
| | 1 | 41 | 41 | 41 | 41 | 37 | 37 | 36 | 36 |

$$
\mathcal{R}_D = \begin{pmatrix} \mathcal{A}_{FF} & & & \\ & \mathcal{A}_{PP} & & \\ & & \frac{1}{2\mu_f}I & \\ & & & \left(\frac{1}{\lambda} + \frac{1}{2\mu_s}\right)I \\ & & & & \left(C_0 + \frac{\alpha^2}{\lambda}\right)I - \frac{\kappa}{\mu_f}\Delta \end{pmatrix}^{-1}. \tag{2.14}
$$

We remark that the first and third blocks of $\mathcal{R}_D$ together define a parameter robust preconditioner for the (standalone) Stokes problem and the remaining blocks form the robust three-field Biot preconditioner [27]. However, in $\mathcal{R}_D$ the sub-problem preconditioners are decoupled.

Alternatively, after observing that the operator $A$ in (2.13a) defines a norm over the velocity-displacement space $\mathbf{H}^1_\star(\Omega_F) \times \mathbf{H}^1_\star(\Omega_P)$ we will also investigate the (block-diagonal) preconditioner

$$
\mathcal{R}_C = \begin{pmatrix} \mathcal{A}_{FF} & \mathcal{A}_{FP} & & \\ \mathcal{A}_{PF} & \mathcal{A}_{PP} & & \\ & & \frac{1}{2\mu_f}I & \\ & & & \left(\frac{1}{\lambda} + \frac{1}{2\mu_s}\right)I \\ & & & & \left(C_0 + \frac{\alpha^2}{\lambda}\right)I - \frac{\kappa}{\mu_f}\Delta \end{pmatrix}^{-1}. \tag{2.15}
$$

We note that in (2.15) the tangential components of the Stokes velocity and of the Biot displacement are coupled. In this sense, the preconditioner captures the interaction between the subsystems and, in particular, the coupling through the Beavers–Joseph–Saffman condition (2.3d).

To investigate the robustness of these preconditioners, we set typical physical parameters in (2.9) except for $\mu_f$ and $\kappa$, which are to be varied. Using a discretization in terms of the lowest-order Taylor–Hood elements (see more details in Section 4.1), we next consider the boundedness of the number of iterations of the preconditioned MinRes solver under mesh refinement and parameter variations. More precisely, using $\mathcal{R}_D$, $\mathcal{R}_C$ (inverted by LU) we compare the number of iterations required for convergence determined by reducing the preconditioned residual norm by a factor $10^8$. The initial vector is taken as random. These initialization and convergence criteria are kept throughout the manuscript.

We report the results in Table 2.1. It can be seen that the number of MinRes iterations produced with the diagonal preconditioner $\mathcal{R}_D$ is rather sensitive to variations in both $\mu_f$ and $\kappa$. In comparison, when fixing $\mu_f = 1$, the iterations appear to be more stable in $\kappa$ when (2.15) is used. However, if $\kappa = 1$ is set, there is a clear deterioration of the performance for small values of $\mu_f$ also with the preconditioner $\mathcal{R}_C$.

The improved performance of the preconditioner $\mathcal{R}_C$, which preserves the tangential coupling of the Stokes and Biot problems in (2.3d), over $\mathcal{R}_D$, where the components are decoupled, suggests to strengthening the coupling (involving the tangential traces) in order to obtain parameter robustness. However, from the point of view of the interface conditions (2.3a)-(2.3d), it is clear that the coupling in the normal direction is missing in $\mathcal{R}_C$.

With the above idea in mind, we proceed to establish well-posedness of (2.9) in the product space equipped with non-standard norms that include additional control at the interface reflecting/arising from the mass conservation condition (2.3a).

## 3. Well-posedness of the Biot–Stokes system

Let us group the variables as $\vec{\boldsymbol{u}} = (\boldsymbol{u}, \boldsymbol{d})$ and $\vec{p} = (p_F, \varphi, p_P)$ and introduce the weighted norm

$$\|(\vec{\boldsymbol{u}}, \vec{p})\|_{\mathbf{H}_\epsilon}^2 := \|\vec{\boldsymbol{u}}\|_A^2 + |\vec{p}|_B^2 + |\vec{p}|_C^2, \tag{3.1}$$

with

$$\|\vec{\boldsymbol{u}}\|_A^2 := 2\mu_f \|\boldsymbol{\epsilon}(\boldsymbol{u})\|_{0,\Omega_F}^2 + \sum_{j=1}^{d-1} \frac{\gamma \mu_f}{\sqrt{\kappa}} \|(\boldsymbol{u} - \boldsymbol{d}) \cdot \boldsymbol{t}_j\|_{0,\Sigma}^2 + 2\mu_s \|\boldsymbol{\epsilon}(\boldsymbol{d})\|_{0,\Omega_P}^2, \tag{3.2a}$$

$$|\vec{p}|_B^2 := \frac{1}{2\mu_f} \|p_F\|_{0,\Omega_F}^2 + \frac{1}{2\mu_s} \|\varphi\|_{0,\Omega_P}^2 + \left(\frac{1}{2\mu_f} + \frac{1}{2\mu_s}\right) \|p_P|_\Sigma\|_{-\frac{1}{2},01,\Sigma}^2, \tag{3.2b}$$

$$|\vec{p}|_C^2 := \frac{1}{\lambda} \|\varphi - \alpha p_P\|_{0,\Omega_P}^2 + C_0 \|p_P\|_{0,\Omega_P}^2 + \frac{\kappa}{\mu_f} \|\nabla p_P\|_{0,\Omega_P}^2, \tag{3.2c}$$

where the fractional norm is defined in (1.5).

In turn, we define the weighted product space $\mathbf{H}_\epsilon$ as the space that contains all $(\vec{\boldsymbol{u}}, \vec{p})$ that are bounded in this norm. The subscript $\epsilon$ encodes the collection of weighting parameters $\kappa, \alpha, \gamma, \mu_f, \mu_s, C_0, \lambda$. Moreover, the space allows for the natural decomposition:

$$\mathbf{H}_\epsilon = \vec{\mathbf{V}}_\epsilon \times \vec{Q}_\epsilon.$$

Thus $\mathbf{V}_\epsilon, Q_\epsilon$ contain all $\vec{\boldsymbol{u}} \in \mathbf{V}$, respectively $\vec{p} \in Q$ (cf. (2.12)) which are bounded in the norms $\vec{\boldsymbol{u}} \mapsto \|\vec{\boldsymbol{u}}\|_A$ and $\vec{p} \mapsto (|\vec{p}|_B^2 + |\vec{p}|_C^2)^{1/2}$.

**Theorem 3.1.** *Problem* (2.9) *is well-posed in the space* $\mathbf{H}_\epsilon$ *equipped with the norm* (3.1). *In other words, the operator* $\mathcal{A} : \mathbf{H}_\epsilon \to \mathbf{H}_\epsilon'$ *in* (2.10) *is a symmetric isomorphism satisfying*

$$\|\mathcal{A}\|_{\mathcal{L}(\mathbf{H}_\epsilon, \mathbf{H}_\epsilon')} \leq C_1, \tag{3.3a}$$

$$\|\mathcal{A}^{-1}\|_{\mathcal{L}(\mathbf{H}_\epsilon', \mathbf{H}_\epsilon)} \leq C_2, \tag{3.3b}$$

*where* $C_1, C_2$ *are positive constants independent of* $\epsilon$.

**Proof.** The operator norm is defined as

$$\|\mathcal{A}\|_{\mathcal{L}(\mathbf{H}_\epsilon, \mathbf{H}_\epsilon')} := \sup_{(\vec{\boldsymbol{u}}, \vec{p}), (\vec{\boldsymbol{v}}, \vec{q})} \frac{\langle \mathcal{A}(\vec{\boldsymbol{u}}, \vec{p}), (\vec{\boldsymbol{v}}, \vec{q}) \rangle}{\|(\vec{\boldsymbol{u}}, \vec{p})\|_{\mathbf{H}_\epsilon} \|(\vec{\boldsymbol{v}}, \vec{q})\|_{\mathbf{H}_\epsilon'}},$$

and condition (3.3a) states the continuity of $\mathcal{A}$. To show this, we first use the Cauchy–Schwarz inequality to derive

$$\langle A\vec{\boldsymbol{u}}, \vec{\boldsymbol{v}} \rangle \leq \|\vec{\boldsymbol{u}}\|_A \|\vec{\boldsymbol{v}}\|_A, \qquad \langle C\vec{p}, \vec{q} \rangle \leq |\vec{p}|_C |\vec{q}|_C. \tag{3.4}$$

It therefore remains to show that $B$ is continuous. Another application of the Cauchy–Schwarz inequality on the different terms together with a trace inequality provides this result.

In order to prove the second relation (3.3b), we aim to verify the assumptions of the Banach–Nečas–Babuška (BNB) theorem (see, e.g., [41]). In particular, we aim to prove that

$$\sup_{(\vec{\boldsymbol{v}}, \vec{p})} \frac{\langle \mathcal{A}(\vec{\boldsymbol{u}}, \vec{p}), (\vec{\boldsymbol{v}}, \vec{q}) \rangle}{\|(\vec{\boldsymbol{v}}, \vec{q})\|_{\mathbf{H}_\epsilon}} \gtrsim \|(\vec{\boldsymbol{u}}, \vec{p})\|_{\mathbf{H}_\epsilon}, \qquad \forall (\vec{\boldsymbol{u}}, \vec{p}) \in \mathbf{H}_\epsilon. \tag{3.5}$$

We do this by assuming that $(\vec{\boldsymbol{u}}, \vec{p}) \in \mathbf{H}_\epsilon$ is given and by constructing an appropriate test function $(\vec{\boldsymbol{v}}, \vec{q}) \in \mathbf{H}_\epsilon$. Following, e.g., [42,27], we choose $\vec{q} = -\vec{p}$ and $\vec{\boldsymbol{v}} = \vec{\boldsymbol{u}}$, giving

$$\langle \mathcal{A}(\vec{\boldsymbol{u}}, \vec{p}), (\vec{\boldsymbol{u}}, -\vec{p}) \rangle = \langle A\vec{\boldsymbol{u}}, \vec{\boldsymbol{u}} \rangle + \langle B\vec{\boldsymbol{u}}, \vec{p} \rangle - \langle B\vec{\boldsymbol{u}}, \vec{p} \rangle + \langle C\vec{p}, \vec{p} \rangle$$
$$= \|\vec{\boldsymbol{u}}\|_A^2 + |\vec{p}|_C^2. \tag{3.6}$$

Lemma 3.1, presented below, allows us to construct $\vec{\boldsymbol{v}}_p$ such that

$$\langle B\vec{\boldsymbol{v}}_p, \vec{p} \rangle = |\vec{p}|_B^2, \qquad \|\vec{\boldsymbol{v}}_p\|_A \leq \beta_0^{-1} |\vec{p}|_B. \tag{3.7}$$

We now use this test function, scaled by a constant $\delta > 0$ to be chosen later, and using (3.2a)-(3.2c) along with (3.4) and (3.7), we derive

$$\langle \mathcal{A}(\vec{\boldsymbol{u}}, \vec{p}), (\delta \vec{\boldsymbol{v}}_p, \vec{0}) \rangle = \langle A\vec{\boldsymbol{u}}, \delta \vec{\boldsymbol{v}}_p \rangle + \delta [B\vec{\boldsymbol{v}}_p, \vec{p}]$$
$$\geq -\delta \|\vec{\boldsymbol{u}}\|_A \|\vec{\boldsymbol{v}}_p\|_A + \delta |\vec{p}|_B^2$$
$$\geq -\frac{1}{2} \|\vec{\boldsymbol{u}}\|_A^2 - \frac{1}{2} \delta^2 \|\vec{\boldsymbol{v}}_p\|_A^2 + \delta |\vec{p}|_B^2$$
$$\geq -\frac{1}{2} \|\vec{\boldsymbol{u}}\|_A^2 + (\delta - \frac{1}{2} \beta_0^{-2} \delta^2) |\vec{p}|_B^2,$$

where we have also used Cauchy–Schwarz and Young's inequality. Setting $\delta = \beta_0^2$ gives us

$$\langle \mathcal{A}(\vec{\boldsymbol{u}}, \vec{p}), (\delta \vec{\boldsymbol{v}}_p, \vec{0}) \rangle \geq -\frac{1}{2} \|\vec{\boldsymbol{u}}\|_A^2 + \frac{1}{2} \beta_0^2 |\vec{p}|_B^2. \tag{3.8}$$

Finally, we take $(\vec{\boldsymbol{v}}, \vec{q}) = (\vec{\boldsymbol{u}} + \delta \vec{\boldsymbol{v}}_p, -\vec{p})$ and put together (3.6) and (3.8) to arrive at

$$\langle \mathcal{A}(\vec{\boldsymbol{u}}, \vec{p}), (\vec{\boldsymbol{v}}, \vec{q}) \rangle \geq \frac{1}{2} \|\vec{\boldsymbol{u}}\|_A^2 + \frac{1}{2} \beta_0^2 |\vec{p}|_B^2 + |\vec{p}|_C^2$$
$$\gtrsim \|(\vec{\boldsymbol{u}}, \vec{p})\|_{\mathbf{H}_\epsilon}^2,$$
$$\|(\vec{\boldsymbol{v}}, \vec{q})\|_{\mathbf{H}_\epsilon}^2 \leq 2 \left( \|(\vec{\boldsymbol{u}}, \vec{p})\|_{\mathbf{H}_\epsilon}^2 + \delta^2 \|\vec{\boldsymbol{v}}_p\|_A^2 \right)$$
$$\leq 2 \left( \|(\vec{\boldsymbol{u}}, \vec{p})\|_{\mathbf{H}_\epsilon}^2 + \beta_0^2 |\vec{p}|_B^2 \right)$$
$$\lesssim \|(\vec{\boldsymbol{u}}, \vec{p})\|_{\mathbf{H}_\epsilon}^2.$$

The combination of these two bounds shows that (3.5) holds. The BNB theorem now provides (3.3b). □

**Lemma 3.1.** *There exists a $\beta_0 > 0$ such that for each $\vec{p} \in \vec{Q}_\epsilon$, a $\vec{\boldsymbol{v}} \in \vec{\mathbf{V}}_\epsilon$ exists that satisfies*

$$\langle B\vec{\boldsymbol{v}}, \vec{p} \rangle = |\vec{p}|_B^2, \qquad \beta_0 \|\vec{\boldsymbol{v}}\|_A^2 \leq |\vec{p}|_B^2.$$

**Proof.** The proof follows similarly to [21, Section 3]. Let $\vec{p} = (p_F, \varphi, p_P) \in \vec{Q}_\epsilon$ be given. We proceed in five steps.

1. With a given total pressure $\varphi$ in the Biot domain, we set up an auxiliary Stokes problem: Find $(\boldsymbol{z}_0, s_0) \in \mathbf{H}^1(\Omega_P) \times L^2(\Omega_P)$ that weakly satisfy

   $$-\operatorname{\mathbf{div}}(\boldsymbol{\epsilon}(\boldsymbol{z}_0) + s_0 \mathbf{I}) = \mathbf{0},$$
   $$\operatorname{div} \boldsymbol{z}_0 = -\varphi \qquad \text{in} \quad \Omega_P,$$

   subject to the mixed boundary conditions

   $$\boldsymbol{z}_0 = \mathbf{0} \text{ on} \quad \Gamma_P^{\boldsymbol{d}} \cup \Sigma, \qquad \text{and} \quad (\boldsymbol{\epsilon}(\boldsymbol{z}_0) + s_0 \mathbf{I}) \, \boldsymbol{n} = \mathbf{0} \text{ on } \Gamma_P^{p_P}.$$

   By the well-posedness of this auxiliary problem (for a proof see, e.g., [40, Chapter I]), the first component of the solution satisfies

   $$\|\boldsymbol{z}_0\|_{1, \Omega_P} \lesssim \|\varphi\|_{0, \Omega_P}.$$

2. We next consider that the trace of $p_P$ is a distribution in $H^{-1/2}(\partial \Omega_P)$, and focus on its restriction to the interface, $p_P|_\Sigma$, belonging to $[H_{01}^{1/2}(\Sigma)]'$ (cf., the end of Section 1).
   Let $\zeta \in H_{01}^{1/2}(\Sigma)$ be the Riesz representative of $p_P|_\Sigma \in [H_{01}^{1/2}(\Sigma)]'$, and consider a Stokes-extension of $\zeta$ into $\Omega_P$ by setting up another auxiliary Stokes problem (and still in the Biot domain): Find a pair $(\boldsymbol{z}_1, s_1) \in \mathbf{H}^1(\Omega_P) \times L^2(\Omega_P)$ that weakly satisfies

   $$-\operatorname{\mathbf{div}}(\boldsymbol{\epsilon}(\boldsymbol{z}_1) + s_1 \mathbf{I}) = \mathbf{0}, \tag{3.10a}$$
   $$\operatorname{div} \boldsymbol{z}_1 = 0 \qquad \text{in} \quad \Omega_P,$$

   subject to the mixed-type boundary conditions

   $$\boldsymbol{z}_1 = \zeta \boldsymbol{n} \text{ on } \Sigma, \tag{3.10b}$$
   $$\boldsymbol{z}_1 = \mathbf{0} \text{ on } \Gamma_P^{\boldsymbol{d}}, \qquad (\boldsymbol{\epsilon}(\boldsymbol{z}_1) + s_1 \mathbf{I}) \, \boldsymbol{n} = \mathbf{0} \text{ on } \Gamma_P^{p_P}.$$

Again, we use the well-posedness of the auxiliary problem (in this case, (3.10)) to conclude that the extension function $\boldsymbol{z}_1$ satisfies a continuous dependence on data

$$\|\boldsymbol{z}_1\|_{1,\Omega_P} \lesssim \|\zeta\|_{\frac{1}{2},01,\Sigma} = \|p_P\|_{-\frac{1}{2},01,\Sigma}.$$

3. We combine the two previous steps to form an auxiliary *Biot velocity* as $\boldsymbol{v}_P := \frac{1}{2\mu_s}(\boldsymbol{z}_0 + \boldsymbol{z}_1)$. By construction, this function has the following properties

$$\begin{aligned}
\langle B(\boldsymbol{v}_P, \boldsymbol{0}), \vec{p}\rangle &= -(\operatorname{div}\boldsymbol{v}_P, \varphi)_{\Omega_P} + \langle \boldsymbol{n}\cdot\boldsymbol{v}_P, p_P\rangle_\Sigma \\
&= \frac{1}{2\mu_s}\left(-(\operatorname{div}\boldsymbol{z}_0, \varphi)_{\Omega_P} + \langle \boldsymbol{n}\cdot\boldsymbol{z}_1, p_P\rangle_\Sigma\right) \\
&= \frac{1}{2\mu_s}\left(\|\varphi\|^2_{\Omega_P} + \|p_P|_\Sigma\|^2_{-\frac{1}{2},01,\Sigma}\right), \\
\|(\boldsymbol{v}_P, \boldsymbol{0})\|^2_A &= 2\mu_s\|\boldsymbol{\epsilon}(\boldsymbol{v}_P)\|^2_{0,\Omega_P} \\
&\leq \frac{1}{2\mu_s}2\left(\|\boldsymbol{z}_0\|^2_{1,\Omega_P} + \|\boldsymbol{z}_1\|^2_{1,\Omega_P}\right) \\
&\lesssim \frac{1}{2\mu_s}\left(\|\varphi\|^2_{\Omega_P} + \|p_P|_\Sigma\|^2_{-\frac{1}{2},01,\Sigma}\right).
\end{aligned}$$

4. Next, we repeat the first three steps with $p_F$ substituted for $\varphi$, $-\zeta$ for $\zeta$, $\Omega_F$ instead of $\Omega_P$ (as well as the relevant boundaries), and $\mu_f$ substituted for $\mu_s$. In particular, for step 2 we note that the Riesz representative $\zeta$ is constructed relatively to $\partial\Omega_P$, but the trace of $\mathbf{H}^1_\star(\Omega_F)$ can be regarded as equivalent to the trace of $\mathbf{H}^1_\star(\Omega_P)$ provided that the shapes and measures of each subdomains are similar (see [43,44], where the argument is applied to a normal velocity trace on the interface). Then, we are allowed to also consider $\zeta \in H^{1/2}_{01}(\Sigma)$ as relative to $\partial\Omega_F$.

   In this case we end up with a *Stokes velocity* $\boldsymbol{v}_F$ satisfying the relations

$$\begin{aligned}
\langle B(\boldsymbol{v}_F, \boldsymbol{0}), \vec{p}\rangle &= \frac{1}{2\mu_f}\left(\|p_F\|^2_{\Omega_F} + \|p_P|_\Sigma\|^2_{-\frac{1}{2},01,\Sigma}\right), \\
\|(\boldsymbol{v}_F, \boldsymbol{0})\|^2_A &\lesssim \frac{1}{2\mu_f}\left(\|p_F\|^2_{\Omega_F} + \|p_P|_\Sigma\|^2_{-\frac{1}{2},01,\Sigma}\right).
\end{aligned}$$

5. For the final step it suffices to combine steps 3 and 4, and choose as test function the pair of functions constructed above $\vec{\boldsymbol{v}} = (\boldsymbol{v}_F, \boldsymbol{v}_P)$, which leads to

$$\langle B\vec{\boldsymbol{v}}, \vec{p}\rangle = |\vec{p}|^2_B, \qquad \|\vec{\boldsymbol{v}}\|^2_A \lesssim |\vec{p}|^2_B. \tag{3.11}$$

Equation (3.11) also contains the right scaling through the use of the $|\cdot|_B$ seminorm. This step concludes the proof. $\quad\square$

According to the general operator preconditioning framework from [25], Theorem 3.1 yields that a parameter-robust preconditioner can be constructed based on the Riesz map $\mathcal{R}: \mathbf{H}'_\epsilon \to \mathbf{H}_\epsilon$ satisfying

$$\|\mathcal{R}\|_{\mathcal{L}(\mathbf{H}'_\epsilon, \mathbf{H}_\epsilon)} \leq 1, \quad \|\mathcal{R}^{-1}\|_{\mathcal{L}(\mathbf{H}_\epsilon, \mathbf{H}'_\epsilon)} \leq 1,$$

which implies that

$$\operatorname{cond}(\mathcal{R}\mathcal{A}) = \|\mathcal{R}\mathcal{A}\|_{\mathcal{L}(\mathbf{H}_\epsilon, \mathbf{H}_\epsilon)}\|(\mathcal{R}\mathcal{A})^{-1}\|_{\mathcal{L}(\mathbf{H}_\epsilon, \mathbf{H}_\epsilon)} \leq C_1 C_2.$$

Following Theorem 3.1 a natural block-diagonal preconditioner for the Biot–Stokes problem is therefore the Riesz map with respect to the inner product in $\mathbf{H}_\epsilon$

$$\mathcal{R} = \begin{pmatrix} \mathcal{A}_{FF} & \mathcal{A}_{FP} & & & \\ \mathcal{A}_{PF} & \mathcal{A}_{PP} & & & \\ \hline & & \frac{1}{2\mu_f}I & & \\ & & & \left(\frac{1}{\lambda} + \frac{1}{2\mu_s}\right)I & -\frac{\alpha}{\lambda}I \\ & & & -\frac{\alpha}{\lambda}I & \left(C_0 + \frac{\alpha^2}{\lambda}\right)I - \frac{\kappa}{\mu_f}\Delta + \frac{1}{\mu}(-\Delta_{\Sigma,01})^{-\frac{1}{2}} \end{pmatrix}^{-1}, \tag{3.12}$$

where we have defined $\mu^{-1} := (2\mu_s)^{-1} + (2\mu_f)^{-1}$. We remark that the fractional operator $(-\Delta_{\Sigma,01})^{-1/2}$ induces a norm on the space $[H^{1/2}_{01}(\Sigma)]'$ (see also [45] for the case of $[H^{1/2}_{00}(\Sigma)]'$).
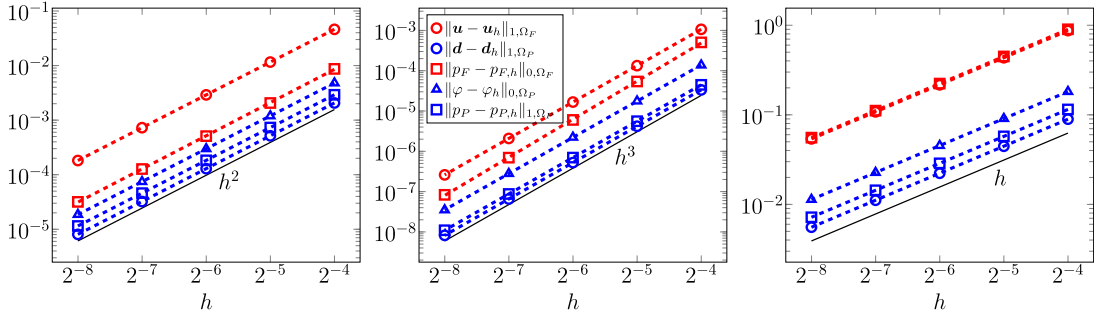
**Fig. 4.1.** Error convergence of the finite element approximation of (2.9) with the manufactured solution (4.1) using (left) TH$_1$, (center) TH$_2$ and (right) CR families for discretization. Theoretically expected convergence rates are observed in all cases. The legend is shared between the subplots.

## 4. Discretization and robust preconditioners for Biot–Stokes

### 4.1. Preliminaries and accuracy verification

In order to define a finite element method for the Biot–Stokes system (2.9) we will use two families of Stokes-stable elements. The generalized Taylor–Hood [46] (TH$_k$, continuous and piecewise polynomials of degree $k + 1$ and degree $k$) type for the pairs [fluid velocity, fluid pressure] and [porous displacement, total pressure], while using continuous and piecewise polynomials of degree $k + 1$ for the porous fluid pressure; as well as non-conforming discretizations based on the lowest-order Crouzeix–Raviart [47] (CR) elements for the pairs [fluid velocity, fluid pressure] and [porous displacement, total pressure], and continuous and piecewise linear elements for the Biot fluid pressure. A requirement is that the meshes for the Biot and Stokes subdomains match at the interface. For sake of completeness, the precise definition of the finite element subspaces is given in Appendix A. We remark that a stable discretization with the CR elements requires additional stabilization for velocity and displacement, e.g., projection stabilization [48], or a facet stabilization [49] which is used in the following. Further details about the discrete formulation with the CR elements are provided in Appendix B.

We recall that, provided that the exact solutions are sufficiently smooth, the theoretical convergence order for the TH$_k$ element is $O(h^{k+1})$ (for Stokes velocity in the $H^1$-seminorm and Stokes pressure in the $L^2$-norm). See, e.g., [50, Sect. 8.8.2], [40, Theorem 2.6], or [46].

Furthermore, we remark that the non-conforming CR element discretization is not covered by the theory presented in this paper and it is, as such, a case of interest.

For the numerical realization of the methods discussed above, we have used the open source finite element library FEniCS [51,52], as well as the specialised module FEniCS$_{ii}$ [53] for handling subdomain- and boundary- restricted terms and variables.

We verify the error decay using the TH$_k$ spaces with polynomial degrees $k = 1, 2$, and the CR family. For this we simply use unity parameters. We consider synthetic forcing terms and boundary data such that the exact manufactured solutions to (2.1) are

$$\boldsymbol{u} = \begin{pmatrix} \cos(\pi x)\sin(\pi y) \\ -\sin(\pi x)\cos(\pi y) \end{pmatrix}, \; p_F = \exp(xy) + \cos(\pi x)\cos(\pi y),$$

$$\boldsymbol{d} = \begin{pmatrix} \cos(\pi x)\sin(\pi y) + \frac{y(x-0.5)}{\lambda} \\ -\sin(\pi x)\cos(\pi y) \end{pmatrix}, \; p_P = \cos(\pi(x^2 + y^2)), \; \varphi = \alpha p_P - \lambda\operatorname{div}\boldsymbol{d}.$$

(4.1)

Note that these exact solutions require non-homogeneous transmission conditions.

We construct a series of uniformly successively refined triangular meshes for $\Omega = (0, 1)^2$, defining the interface as the segment $\{0.5\} \times (0, 1)$ and considering the left half of the domain as $\Omega_F$ and the right half as $\Omega_P$. Then, we proceed to measure individual errors between closed-form and approximate solutions in the usual norms

$$e(\boldsymbol{u}) = \|\boldsymbol{u} - \boldsymbol{u}_h\|_{1,\Omega_F}, \quad e(p_F) = \|p_F - p_{F,h}\|_{0,\Omega_F},$$

$$e(\boldsymbol{d}) = \|\boldsymbol{d} - \boldsymbol{d}_h\|_{1,\Omega_P}, \quad e(\varphi) = \|\varphi - \varphi_h\|_{0,\Omega_P}, \quad e(p_P) = \|p_P - p_{P,h}\|_{1,\Omega_P}.$$

Fig. 4.1 reports the approximation errors for the three discretizations. In all cases the expected order $k + 1$ for TH$_k$ can be observed. For the CR family we obtain the expected linear convergence.

Having defined suitable finite element discretization for the Biot–Stokes system, we next investigate robustness of the fractional preconditioner (3.12) which was established theoretically in Theorem 3.1 with the assumption of specific boundary conditions on the sub-boundaries intersecting the interface, namely, that $\Sigma$ meets the intersection between the Biot displacement and the Stokes velocity boundaries. However, the theory and in turn the $\mathcal{R}$ preconditioners can be extended to more general boundary conditions as we will demonstrate by the numerical experiments. In particular, in Section 4.4

we consider the setup where the interface intersects boundaries $\Gamma_F^{\sigma}$, $\Gamma_P^{p_P}$ see Fig. 1.1. Then, in Section 4.6 the interface is a closed curve.

Due to the Laplace operator on the interface, the discretization of preconditioners $\mathcal{R}$ (3.12) is not immediately evident. Before discussing the results let us therefore comment on the construction of the critical component, that is, the fractional operators.

### 4.2. Discrete preconditioner

From (3.12) we observe that in the pressure block of the preconditioner $\mathcal{R}$ the operator acting on $(\varphi, p_P)$,

$$\begin{pmatrix} \left(\frac{1}{\lambda} + \frac{1}{2\mu_s}\right)I & -\frac{\alpha}{\lambda}I \\ -\frac{\alpha}{\lambda}I & \left(C_0 + \frac{\alpha^2}{\lambda}\right)I - \frac{\kappa}{\mu_f}\Delta + \mu^{-1}(-\Delta_{\Sigma,01})^{-\frac{1}{2}} \end{pmatrix}^{-1}, \tag{4.2}$$

contains a sum of a bulk term coupling the two pressures and a fractional interface term $\mu^{-1}(-\Delta_{\Sigma,01})^{-1/2}$. Thus, the action of the operator implicitly involves the trace of the Biot pressure at the interface $\Sigma$. In the discrete setting, mirroring this property requires a discrete trace space $S_h$ and a restriction operator. In the following we choose $S_h$ as the space of piecewise continuous polynomials of order $k+1$ whenever the $\text{TH}_k$ family is used. For the CR family, $S_h$ is constructed from piecewise continuous linear functions. The restriction operator is then realized as an $L^2$-projection.

Once on the interface we approximate the fractional operator based on the spectral decomposition, see, e.g., [54]. That is,

$$\langle \mu^{-1}(-\Delta_{\Sigma,01})^{-1/2}u, v\rangle_{\Sigma} := \sum_i \lambda_i^{-1/2}(\mu^{-1}u_i, u)_{\Sigma}(\mu^{-1}u_i, v)_{\Sigma} \quad \forall u, v \in S_h, \tag{4.3}$$

where $(u_i, \lambda_i) \in S_h \times \mathbb{R}$ are solutions of the generalized eigenvalue problem

$$(\mu^{-1}\nabla u_i, \nabla v)_{\Sigma} = \lambda_i(\mu^{-1}u_i, v)_{\Sigma} \quad \forall v \in S_h, \tag{4.4}$$

satisfying the orthogonality condition $(\mu^{-1}u_i, u_j)_{\Sigma} = \delta_{ij}$. Note that in (4.4) the Dirichlet boundary conditions are prescribed on $\partial\Sigma$ reflecting the trace spaces of velocity and displacement when $\Gamma_F^{\boldsymbol{u}}$ and $\Gamma_P^{\boldsymbol{d}}$ are incident to $\Sigma$ (as was assumed in Theorem 3.1).

**Remark 4.1** *(Approximate fractional norms).* In the context of finite element error estimation, the fractional order norms are often replaced by discrete approximations, e.g. the norm of $\left[H_{01}^{1/2}(\Sigma)\right]'$ is approximated by weighted $L^2$ norm as $q \mapsto \|h^{1/2}q\|_{0,\Sigma}$, see [55,56]. The appeal of such approximations for preconditioning is then that the potentially expensive fractional operator (and the eigenvalue problem (4.4)) is avoided. However, as we shall illustrate next, the discrete norms in general do not lead to robust preconditioners.

In Fig. 4.2 we consider the modified preconditioners (3.12) where the fractional block $(-\Delta_{\Sigma,01})^{-1/2}$ is replaced by $h^t I_{\Sigma}$, $t = -1, 0, 1$ where $h$ is the mesh size on $\Sigma$. That is, for $t = 0$ the block is simply discretized into a mass matrix on the interface while $t = 1$ induces the discrete approximation to a norm on $\left[H_{01}^{1/2}(\Sigma)\right]'$. Considering the setup (geometry and Krylov solver settings) of Example 2.1 with unit parameters except for the permeability $\kappa$ and $\text{TH}_1$ discretization, it can be seen that $hI_{\Sigma}$ leads to iterations bounded in mesh size for large values of $\kappa$ ($\kappa = 1$ in the figure). However, for small $\kappa$ the iterations stabilize under mesh refinement only for sufficiently small mesh sizes. The iterations are thus sensitive to parameters. We remark that $t < 1$ seems to lead to an increased parameter sensitivity.

Going beyond the theoretical analysis, we demonstrate in Section 4.4 that for the configuration with $\Gamma_F^{\sigma}$, $\Gamma_P^{p_P}$ intersected by the interface, the operator (4.2) (and in turn the preconditioner (3.12)) needs to be modified. Specifically, the fractional term then reads $\mu^{-1}(-\Delta_{\Sigma} + I_{\Sigma})^{-1/2}$. The operator is defined analogously to (4.3), where, in contrast, the $H^1$-norm (cf. the $H^1$-seminorm in (4.4)) is now used in the eigenvalue problem: Find $(u_i, \lambda_i) \in (S_h, \mathbb{R})$ such that

$$(\mu^{-1}\nabla u_i, \nabla v)_{\Sigma} + (\mu^{-1}u_i, v)_{\Sigma} = \lambda_i(\mu^{-1}u_i, v)_{\Sigma} \quad \forall v \in S_h, \tag{4.5}$$

and $(\mu^{-1}u_i, u_j)_{\Sigma} = \delta_{ij}$. Note that here the Neumann boundary conditions are prescribed on $\partial\Sigma$.

We remark that the fractional operators and in particular the boundary conditions in (4.4) and (4.5) must be set based on the configuration of the boundaries with respect to the interface. The fact that the conditions cannot be chosen freely is investigated next in Example 4.1 together with the observation that parameter stability of the preconditioners (3.12) is affected by enforcement of Dirichlet boundary conditions in construction of the fractional operators via the eigenvalue problems (4.4) and (4.5).
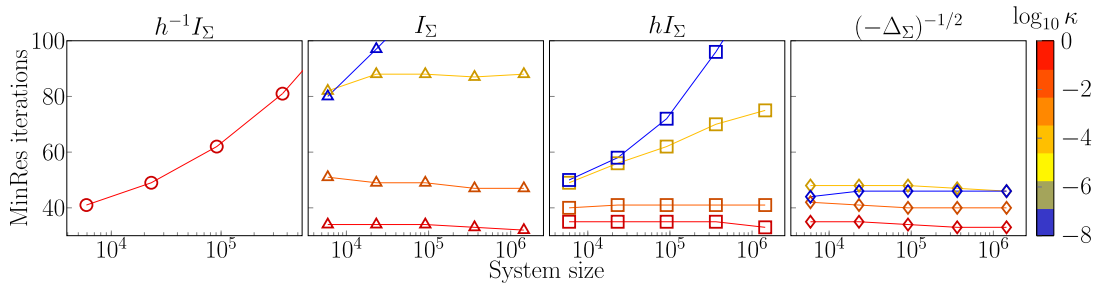
**Fig. 4.2.** Modified Biot-Stokes preconditioners (3.12) with the fractional operator replaced by weighted identity (from left to right) $h^t I_\Sigma$, $t = -1, 0, 1$. Setup of Example 2.1 is used with $\kappa$ varied while other parameters are held fixed at 1. Discretization by TH$_1$ elements. MinRes iterations under mesh refinement and different values of $\kappa$ are shown. Missing values (in first three subfigures) indicate lack of convergence in under 100 iterations. The considered approximations to the fractional term do not yield parameter robustness. For reference, performance with the preconditioner (3.12) is given in the rightmost subfigure.

**Example 4.1** *(Boundary conditions in fractional operators).* In the following, given the geometry of Example 2.1, let $C_0 = 0$, $\kappa = 10^{-10}$ while the remaining problem parameters of the Biot–Stokes system (2.9) are set to unity. This choice is made to put emphasis on the fractional term in the preconditioner (3.12).

Assuming first that $\Sigma$ intersects $\Gamma_F^\sigma$ and $\Gamma_P^{p_P}$, we consider (2.9) either with a preconditioner (3.12), where Dirichlet boundary conditions are (strongly) enforced on the fractional operator, or a modified preconditioner which uses the operator $\mu^{-1}(-\Delta_\Sigma + I_\Sigma)^{-1/2}$ constructed with the Neumann boundary conditions, see (4.5). Using a discretization by TH$_1$ we observe in Table 4.1 that the Dirichlet conditions result in a lack of boundedness in the mesh size. On the other hand, when Neumann boundary conditions are imposed on the fractional operator the spectral condition numbers of the preconditioned problem seem to converge along with mesh refinement.

Repeating the experiment for the configuration where the interface is incident to $\Gamma_F^{\boldsymbol{u}}$ and $\Gamma_P^{\boldsymbol{d}}$, it can be seen that Neumann boundary conditions lead to a growth similar to what was observed in the previous setup with Dirichlet datum. Furthermore, in Table 4.1 the condition numbers blow up also with $\mu^{-1}(-\Delta_{\Sigma,01})^{-1/2}$. However, in this case the growth can be traced to the (two) eigenvalues that correspond to the degrees of freedom[6] of the space $S_h$ on $\partial\Sigma$ which are set strongly by the Dirichlet boundary conditions. This observation motivates using the Nitsche technique [57] in order to enforce the conditions on $\mu^{-1}(-\Delta_{\Sigma,01})^{-1/2}$. With a suitably chosen Nitsche penalty parameter, Table 4.1 (column D$_{\text{Nitsche}}$) reveals that (3.12) yields mesh independence.

The fact that for $\Sigma$ intersecting $\Gamma_F^{\boldsymbol{u}}$ and $\Gamma_P^{\boldsymbol{d}}$ the numerical issues with Dirichlet boundary conditions of the fractional operators are related to their strong enforcement, can be further illustrated using a discretization for which the intermediate trace space $S_h$ has no degrees of freedom on the boundary $\partial\Sigma$. To this end, we here consider a modification of the CR family where the Biot fluid pressure space is made of piecewise constants. The discrete Laplace operator in (2.9) as well as in the eigenvalue problem (4.4) is then defined analogously to the finite volume method, and in particular utilizing two-point flux approximation, see, e.g., [58]. After using $\mu^{-1}(-\Delta_{\Sigma,01})^{-1/2}$ with Dirichlet boundary conditions enforced weakly, stable condition numbers are achieved, as observed in column CR$^\sharp$ of Table 4.1.

In order to show that strong enforcement of the Dirichlet boundary conditions can be used depending on the boundary configuration, we finally consider a setup where the interface meets $\Gamma_F^{\boldsymbol{u}}$ on the Stokes side while on the incident Biot boundary (which we denote by $\Gamma_P^\dagger$) we assume Dirichlet data on the displacement $\boldsymbol{d}$ and on the pressure $p_P$. Then, using a TH$_1$ discretization together with the preconditioner (3.12), bounded condition numbers are produced, which can be observed in the last column of Table 4.1.

We finally remark that the spectral realization (4.3) is not scalable to problems where the interface and the trace space are large. However, the representation is well suited for the applications pursued here, specifically the robustness study where we are interested in exact (inverted by LU) preconditioners.

### 4.3. Parameter sensitivity

We demonstrate robustness of the fractional preconditioner (3.12) by a sensitivity study where the physical parameters in (2.9) are varied such that $10^{-9} \le \mu_f, \kappa \le 1$, $1 \le \lambda \le 10^{12}$, $10^{-2} \le \gamma \le 10^2$, $10^{-8} \le \alpha \le 1$. Since $\mu_s$ is commonly used for rescaling we fix its value to 1. Moreover, the storage capacity is set to 0 as this is the more challenging limit of the parameter's range. The chosen parameter ranges are motivated by applications of the Biot-Stokes type models in brain mechanics where the models are used at various scales. For example, in large scale applications (see later Section 4.6), the characteristic length scale is decimeter as e.g. in [59,60,28] whereas other applications are of micron scale [61–63]. As such,

---

[6] The number of unbounded modes is finite (and independent of refinement) when $\Sigma$ is a curve. However, when the interface is a manifold in 3$d$ the number of unbounded modes grows with $h$ (as $\partial\Sigma$ is refined).

**Table 4.1**

Spectral condition numbers for the Biot–Stokes problem (2.10) with fractional preconditioners (3.12). Boundary condition configurations from Fig. 1.1 are considered; $\Sigma$ intersects $\Gamma_F^\sigma$ and $\Gamma_P^{p_P}$ or $\Gamma_P^u$ and $\Gamma_P^d$. In addition, on $\Gamma_P^\dagger$ we prescribe both $\boldsymbol{d}$ and $p_P$. The fractional preconditioners differ by the boundary conditions enforced on $\partial\Sigma$; Dirichlet condition, cf. (4.4), enforced strongly (D) or with Nitsche's method (D$_{\text{Nitsche}}$) or Neumann condition (N), cf. (4.5). Systems are discretized by TH$_1$ family except for CR$^\sharp$ where the *modified* CR family is used with the Biot pressure space constructed from piecewise constant functions. For the finest refinement level the discrete linear system contains approximately 350 thousand degrees of freedom.

| $\log_2 h^{-1}$ | $\Gamma_F^\sigma, \Gamma_P^{p_P}$ | | $\Gamma_F^u, \Gamma_P^d$ | | | | $\Gamma_F^u, \Gamma_P^\dagger$ |
|---|---|---|---|---|---|---|---|
| | D | N | D | N | D$_{\text{Nitsche}}$ | D with CR$^\sharp$ | D |
| 2 | 10.61 | 16.67 | 3369 | 24.48 | 7.02 | 8.07 | 6.77 |
| 3 | 12.17 | 17.58 | 13879 | 30.29 | 7.43 | 8.45 | 7.31 |
| 4 | 13.90 | 18.12 | 56254 | 35.91 | 7.59 | 8.60 | 7.53 |
| 5 | 15.73 | 18.53 | – | 41.66 | 7.67 | 8.60 | 7.64 |
| 6 | 17.63 | 18.83 | – | 47.66 | 7.71 | 8.57 | 7.69 |
| 7 | 19.58 | 19.06 | – | 53.96 | 7.72 | 8.54 | 7.71 |

**Table 4.2**

Number of MinRes iterations for Biot-Stokes problem from Example 2.1 and unit parameters. Discretization by TH$_1$ elements. Preconditioning by block-diagonal preconditioner (3.12) and preconditioner (4.6) is considered. Convergence is determined by reducing the preconditioned residual norm by factor $10^8$. The solvers are started from a random initial vector.

| $|H_{\epsilon,h}|$ | 5927 | 23111 | 91271 | 362759 |
|---|---|---|---|---|
| $\mathcal{R}_F$ (4.6) | 13 | 12 | 12 | 12 |
| $\mathcal{R}$ (3.12) | 35 | 34 | 34 | 33 |

for instance the value of the permeability which scales as m$^2$ will change by 10 orders of magnitude (from dm$^2$ to μm$^2$) depending on the application. Further, the elastic parameters scale linearly with the length scale whereas for instance the storage coefficient scales inversely with the length scale. For a review of parameters, consider [64,65].

The Biot–Stokes system is then considered on the geometry from Example 2.1 with the boundary configuration satisfying the assumptions in Theorem 3.1. That is, the interface intersects $\Gamma_F^u$ on the Stokes side and $\Gamma_P^d$ on the Biot side. In turn, the fractional operator is constructed as given in (4.3). Finally, following Example 2.1, the convergence criterion for the MinRes solver is a reduction of the preconditioned residual norm by factor $10^8$. As we are here interested in performance of the exact preconditioner, the action of (3.12) is computed by LU factorization of the $2 \times 2$ velocity-displacement and the $3 \times 3$ pressure blocks, respectively. Because of LU limitations, we restrict our experiments to lowest order discretizations, i.e. only TH$_1$ and CR families are considered. However, we did not observe any noticeable deterioration of performance (i.e., lack of boundedness in mesh size or parameter variations) with higher order elements.

Using TH$_1$ elements, Figs. 4.3 and 4.4 present slices of the explored parameter space. More precisely, in each subplot column-indexed by fixed value of $\mu_f$ and row-indexed by scalar permeability $\kappa$ we plot dependence of the MinRes iterations on system size for varying Lamé parameter $\lambda$ (indicated by color), the Biot-Willis coefficient $\alpha$ (in Fig. 4.3, $\gamma$ is set to 1) and the slip-rate coefficient $\gamma$ (in Fig. 4.4, $\alpha$ is set to 1). We observe that for each of the parameter combinations the MinRes iterations are bounded in mesh size. In addition, the solver converges in 21-56 iterations despite the large parameter variations spanning several orders of magnitude. These results demonstrate the robustness of preconditioner (3.12) in material and discretization parameters.

**Remark 4.2** (*Triangular preconditioners*). The Schur complement preconditioner in the block diagonal operator $\mathcal{R}$ in (3.12) can be utilized to construct more involved upper/lower triangular preconditioners [66] or full factorization preconditioners [67, 68], which are known to yield convergence in fewer Krylov iterations. Here we illustrate the potential savings by considering the latter preconditioner type, namely,

$$\mathcal{R}_F := \mathcal{B}_U \mathcal{R} \mathcal{B}_U', \quad \mathcal{B}_U := \begin{pmatrix} I & -A^{-1}B' \\ & I \end{pmatrix}. \tag{4.6}$$

We recall that the operators $A$ and $B$ are defined in (2.13). Note also that the product $\mathcal{B}_U \mathcal{R}$ defines the upper block triangular preconditioner of [66].

The symmetric preconditioner (4.6) allows for using the MinRes Krylov solver and thus a direct comparison with the block-diagonal preconditioner (3.12). Using unit parameters and the setup of Example 2.1, the iteration counts required for convergence are reported in Table 4.2. The full factorization preconditioner converges in less than half the number of iterations. Though the single application of (4.6) is more costly than that of (3.12), the fewer iterations in this case translate to faster compute times.
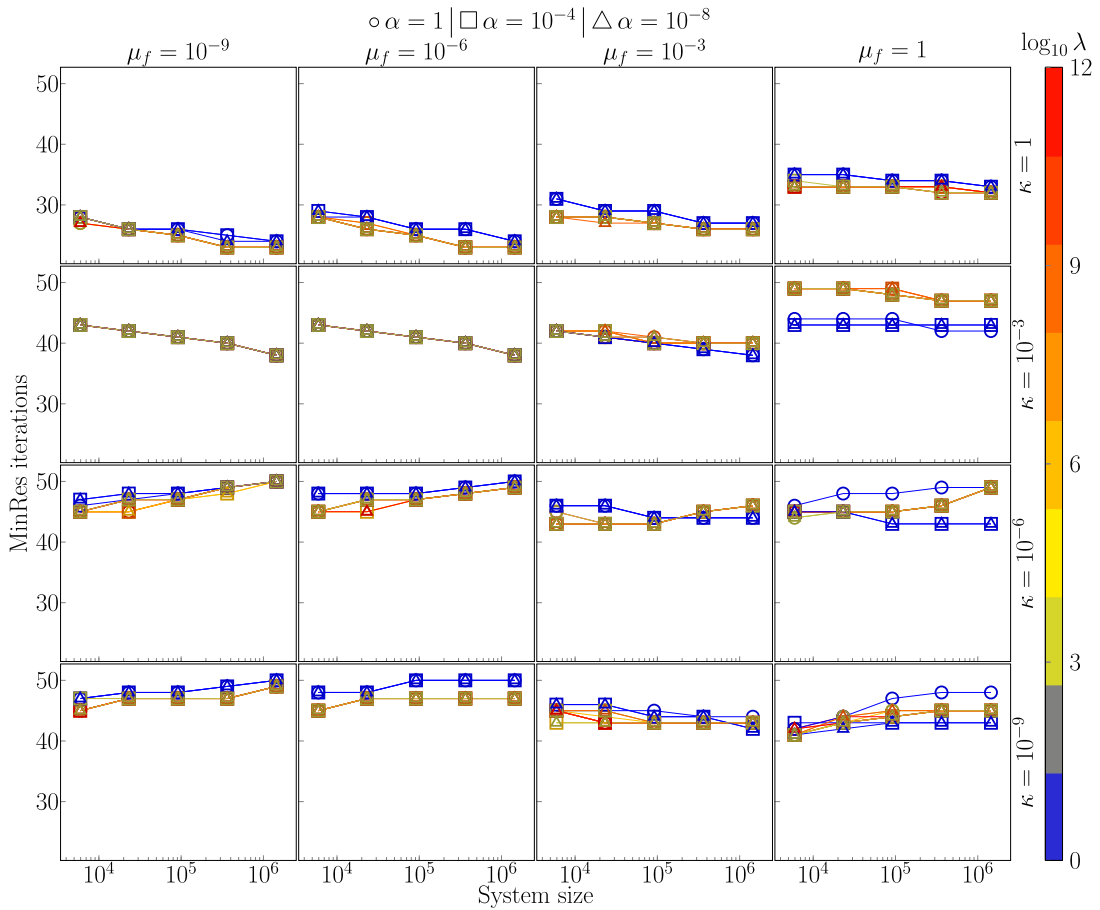
**Fig. 4.3.** Performance of the Biot–Stokes preconditioner (3.12). Geometry of Example 2.1 is used with $\Sigma$ intersecting $\Gamma_F^{\boldsymbol{u}}$ and $\Gamma_P^{\boldsymbol{d}}$. We set $\mu_s$, $\gamma$ to 1 while $C_0 = 0$. The parameters $\mu_f$, $\kappa$, $\lambda$, $\alpha$ are varied. Values of the Biot-Willis coefficient are indicated by markers. In this case, the discretization uses TH$_1$ elements.

### 4.4. Other boundary configurations

The Biot–Stokes preconditioner (3.12) can be extended beyond the boundary configurations assumed in the theoretical analysis, namely, the requirement that $\Sigma$ is incident to $\Gamma_F^{\boldsymbol{u}}$ and $\Gamma_P^{\boldsymbol{d}}$. We illustrate this here by letting the interface intersect the boundaries $\Gamma_F^{\boldsymbol{\sigma}}$, $\Gamma_P^{p_P}$. Following Section 4.2, the configuration leads to the fractional operator $\mu^{-1}(-\Delta_\Sigma + I_\Sigma)^{-1/2}$, see (4.5).

Employing the experimental setup of Section 4.3 the performance of the (4.5)-adapted preconditioner (3.12) is illustrated in Fig. 4.5 where the slice of the parameter space for $C_0 = 0$, $\gamma = 1$ is shown (cf. Fig. 4.3 where $\Gamma$ is incident to $\Gamma_F^{\boldsymbol{u}}$ and $\Gamma_P^{\boldsymbol{d}}$). For all the tested parameter values the preconditioner led to convergence in 23 to 58 iterations thus indicating that $\mathcal{R}$ is indeed parameter robust and mesh independent.

For CR family, the MinRes iterations are reported in Fig. B.2. Here, for the sake of brevity we present results only for the stronger tangential coupling, i.e., $\gamma$ is fixed at $10^2$ and we explore robustness for varying $\mu_f$, $\kappa$, $\lambda$ and $\alpha$. It can be seen that the fractional preconditioner leads to convergence in 22–57 iterations for all the parameter combinations considered. We remark that the stability of CR discretization for the three-field Biot formulation is explored in Appendix B.

### 4.5. Diagonal pressure preconditioner

From the point of view of computational efficiency a possible drawback[7] of preconditioner (3.12), is the fact that due to the $C$-seminorm in (3.1) the pressure block contains a $2 \times 2$ operator (4.2). However, for the three-field Biot problem, the authors in [27] show that parameter robustness can be obtained also if $(\varphi, p_P)$ are controlled in a simpler norm, cf. the Biot block of the operator $\mathcal{R}_D$ in (2.14). Following this observation we next consider a Biot–Stokes preconditioner of the form

---

[7] In addition to the presence of the fractional operator on the interface.
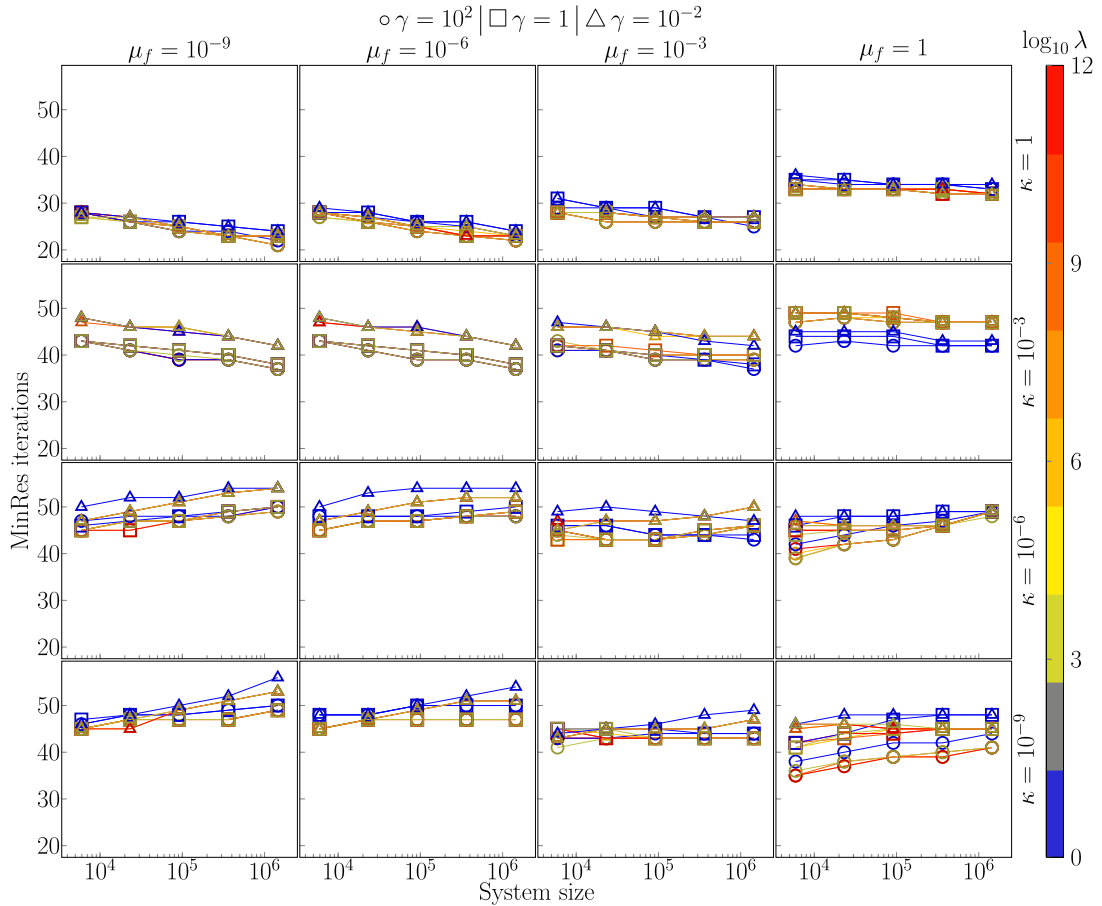
**Fig. 4.4.** Performance of the Biot–Stokes preconditioner (3.12). The problem is setup on the geometry from Example 2.1 with boundary conditions prescribed such that $\Sigma$ intersects $\Gamma_F^{\boldsymbol{u}}$ and $\Gamma_P^{\boldsymbol{d}}$. We set $\mu_s$, $\alpha$ to 1 while $C_0 = 0$. Parameters $\mu_f$, $\kappa$, $\lambda$, $\gamma$ are varied. Values of the slip-rate coefficient $\gamma$ are indicated by markers. A discretization by $TH_1$ is used.

$$
\tilde{\mathcal{R}} = \begin{pmatrix} \mathcal{A}_{FF} & \mathcal{A}_{FP} & & & \\ \mathcal{A}_{PF} & \mathcal{A}_{PP} & & & \\ & & \frac{1}{2\mu_f}I & & \\ & & & \left(\frac{1}{\lambda}+\frac{1}{2\mu_s}\right)I & \\ & & & & \left(C_0+\frac{\alpha^2}{\lambda}\right)I - \frac{\kappa}{\mu_f}\Delta + \frac{1}{\mu}(-\Delta_{\Sigma,01})^{-\frac{1}{2}} \end{pmatrix}^{-1}, \tag{4.7}
$$

and we note that the pressure block is diagonal.

Using the computational setup of Section 4.3 we compare the preconditioner (3.12) derived in Theorem 3.1 with the [27]-inspired operator $\tilde{\mathcal{R}}$ defined in (4.7). For the simple geometry of Example 2.1 we set $\mu_s = 1$, $\gamma = 1$, $C_0 = 0$ while the remaining parameters are varied. As before, uniform grid refinements and discretization by $TH_1$ elements were used. The preconditioners are compared in Fig. 4.6 where we report the number of preconditioned MinRes iterations required for convergence (determined by reducing the preconditioned residual norm of a random initial vector by a factor of $10^8$). Here, both preconditioners were inverted exactly by LU. We observe that the performance of the preconditioners in terms of iteration counts is practically identical, except for $\lambda = 1$, $\alpha = 1$ where (4.7) requires more iterations (about 20) for convergence.

### 4.6. Interfacial flow in the brain

In the examples presented thus far the fractional preconditioners were applied to the Biot–Stokes problem posed in geometries where the interface formed a simple curve (a straight segment in fact). In addition, the number of degrees of freedom associated with $\Sigma$, and in turn the discrete fractional operators, were small. To apply the proposed fractional preconditioners in a more practical setting our final example concerns the interfacial flow in a brain. The chosen problem
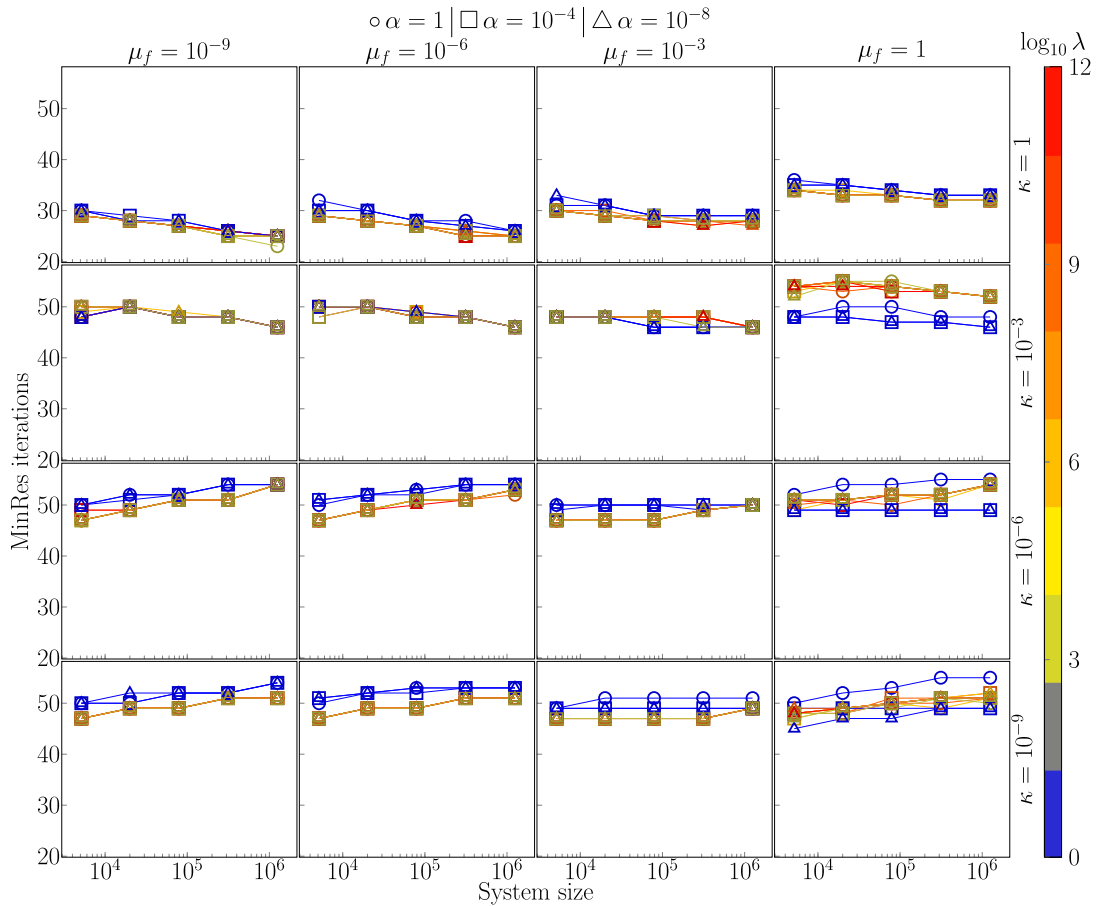
**Fig. 4.5.** Performance of the Biot–Stokes preconditioner (3.12). Geometry of Example 2.1 is used with $\Sigma$ intersecting $\Gamma_F^\sigma$ and $\Gamma_P^{p_P}$. The fractional operator is changed to $\mu^{-1}(-\Delta_\Sigma + I_\Sigma)^{-1/2}$. We set $\mu_s$, $\gamma$ to 1 while $C_0 = 0$. The parameters $\mu_f$, $\kappa$, $\lambda$, $\alpha$ are varied. Values of the Biot-Willis coefficient are indicated by markers. In this case, the discretization uses TH$_1$ elements.

is motivated by applications such as the modeling of the glymphatic system [69] where poro-elastic models of the brain interact with the surrounding cerebrospinal fluid [70]. Here, e.g. cardiac pulsations [71] create pressure pulsations in the cerebrospinal fluid that surrounds the brain, which again propagate through the poroelastic brain. Notably, the interface between the viscous and poroelastic domains are large and complex.

As realistic brain geometries currently cannot be tackled with our spectral approach (4.3) due to the size of the interface,[8] we choose the problem geometry as two-dimensional slices, see Fig. 4.7. The chosen axial and coronal geometries[9] could in principle be used in simplified simulations of hemorrhage or the effects of incoming cerebrospinal fluid flow from the spinal canal. For relevance in real applications, however, three-dimensional geometries/simulations would be needed. Here the 2$d$ geometries are thus primarily used to investigate performance of our preconditioners in a more practical setting with large and irregularly shaped interface and realistic parameter values. In addition, differing from the assumptions of the theoretical analysis in Section 3, the geometries lead to closed interfaces.

We then model flow of a water-like fluid in free-flow domain that is the space surrounding the brain known as the subarachnoid space and in the poroelastic domain that is the brain parenchyma. We remark that the interface thus forms a closed surface. The material parameters of the Biot model are adapted from [64,59]. We let $\mu_f = 1 \cdot 10^{-3}$ Pa $\cdot$ s, $\alpha = 1$, $C_0 = 2 \cdot 10^{-5}$ Pa$^{-1}$ while the slip-rate coefficient is set as $\gamma = 1$. Finally, the Lamé constants are based on the Young modulus 16 kPa and the Poisson ratio of 0.48.

---

[8] The coarsest yet still reasonably well resolved surface mesh of a 3$d$ brain at our disposal has circa 50 thousand cells. The resulting eigenvalue problem is roughly 4 times larger than what can be computed on a computer with 24GB RAM.

[9] We generate the meshes based on smoothed slices of a real brain. The scripts for creating and meshing the coronal and axial geometries, together with the required input data can be found at https://github.com/MiroK/slash/blob/master/demos/get_coronal_mesh.py and https://github.com/MiroK/slash/blob/master/demos/get_axial_mesh.py.
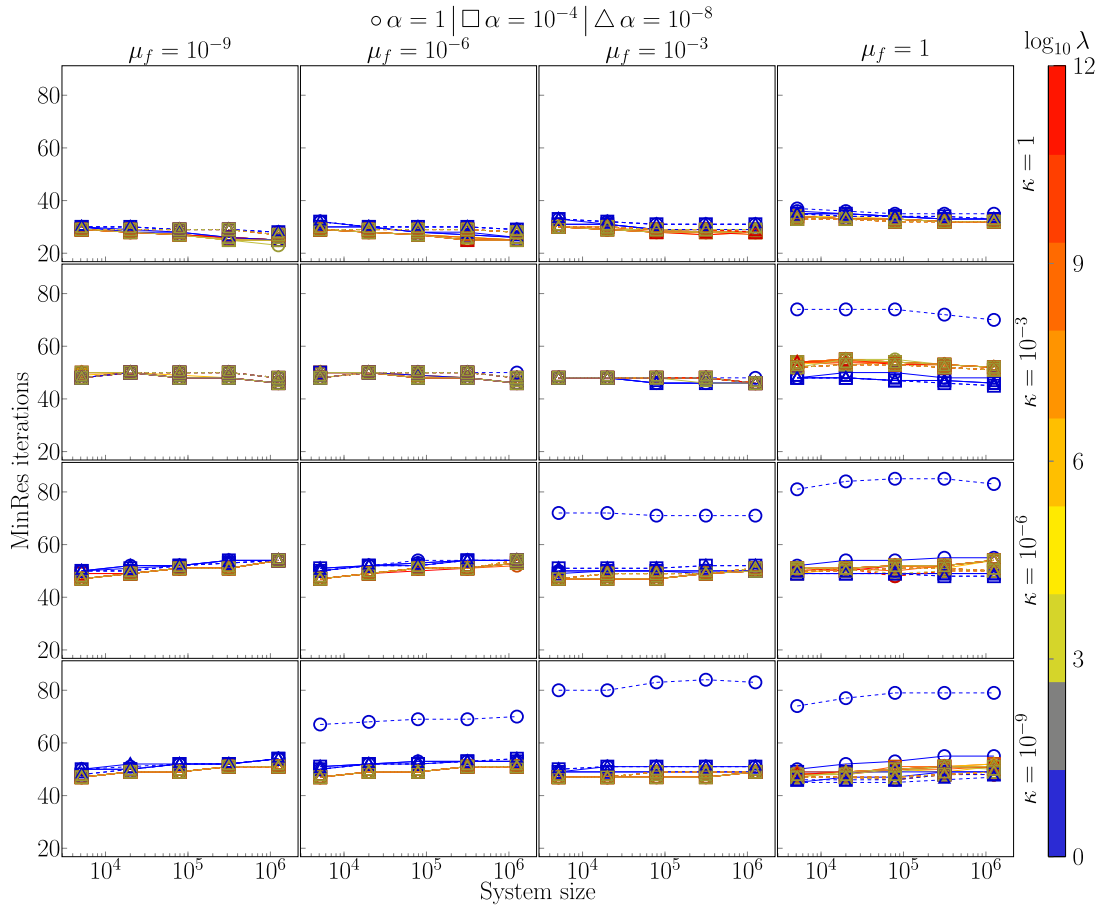
**Fig. 4.6.** Number of MinRes iterations required for solving the Biot-Stokes problem with geometry from Example 2.1 and $\Sigma$ intersecting $\Gamma_F^\sigma$ and $\Gamma_P^{p_p}$. Two preconditioners are compared: the theoretically established operator (3.12) (solid lines) and $\tilde{\mathcal{R}}$ from (4.7) (dashed lines). We set $\mu_s$, $\gamma$ to 1 while $C_0 = 0$. The parameters $\mu_f$, $\kappa$, $\lambda$, $\alpha$ are varied. Values of the Biot-Willis coefficient are indicated by markers. Uniform refinements of the initial mesh are considered and the system is discretized by TH$_1$ elements. The interface/boundary configuration requires modification of the fractional operator which is changed to $\mu^{-1}(-\Delta_\Sigma + I_\Sigma)^{-1/2}$ in both preconditioners. Except for cases where $\lambda = 1$, $\alpha = 1$, performance of the preconditioners is practically identical.

**Table 4.3**
MinRes iterations with different preconditioners for the Biot-Stokes problem from Section 4.6 and two-dimensional geometries from Fig. 4.7. The solvers are stared random initial guess and terminate once the preconditioned residual norm is reduced by $10^8$. Gradually refined meshes of the geometry are generated with mesh size in mm given in the $h$ column of the table. Dimensionalities of the corresponding finite element solution space based on TH$_1$ elements are shown together with the size of the trace space $S_h$, cf. Section 4.2. The fractional preconditioner (3.12) leads to bounded iterations, and also fewer iterations are required compared to the simple preconditioners from Example 2.1.

| | Axial | | | | | Coronal | | | | |
|---|---|---|---|---|---|---|---|---|---|---|
| $h$ [mm] | $|\mathbf{H}_{\epsilon,h}|$ | $|S_h|$ | $\mathcal{R}$ | $\mathcal{R}_D$ | $\mathcal{R}_C$ | $h$ [mm] | $|\mathbf{H}_{\epsilon,h}|$ | $|S_h|$ | $\mathcal{R}$ | $\mathcal{R}_D$ | $\mathcal{R}_C$ |
| 3.21 | 12919 | 266 | 77 | 445 | 98 | 2.46 | 11681 | 178 | 80 | 406 | 106 |
| 1.93 | 41545 | 530 | 75 | 473 | 104 | 1.67 | 36677 | 355 | 85 | 435 | 116 |
| 1.05 | 134980 | 1066 | 81 | 513 | 114 | 0.86 | 132775 | 710 | 88 | 446 | 121 |
| 0.53 | 482371 | 2118 | 83 | 525 | 119 | 0.44 | 496680 | 1420 | 86 | 440 | 124 |
| 0.27 | 1840764 | 4234 | 82 | 521 | 119 | 0.21 | 1895459 | 2838 | 85 | 435 | 121 |

For both axial and coronal geometry the boundary of the outer spaces is assumed impermeable with $\boldsymbol{u} = \boldsymbol{0}$ prescribed on most of the surface, except for regions (marked with red and orange in Fig. 4.7, left) where traction is set in order to drive the flow.

We discretize the system by TH$_1$ elements in order to reduce the number of unknowns on the interface such that the eigenvalue problem (4.5) as well as LU inverse of the preconditioner blocks remain computationally tractable.[10] For each level of (uniform) refinement the flow problem is then solved by a preconditioned MinRes solver starting from a random initial vector with relative tolerance of $10^{-8}$. As the preconditioner (3.12) is used, where the fractional term reads

---

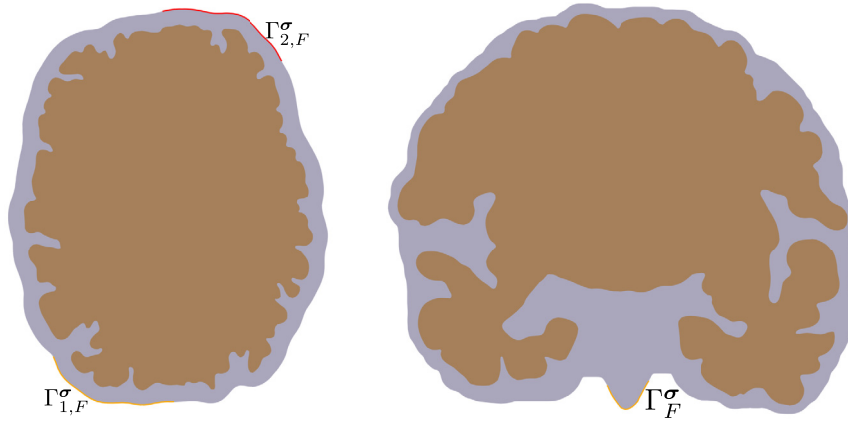[10] Specifications of our hardware setup used can be found Section 4.7.

**Fig. 4.7.** Idealized brain sized geometries (plotted not-to-scale). The brain is enclosed in a water-filled fluid space. For axial slice (left) $|\Sigma| \approx 690$ mm, $|\Gamma_F^{\boldsymbol{u}}| \approx 391$ mm, $|\Gamma_F^{\boldsymbol{\sigma}}| \approx 140$ mm while in coronal slice (right) $|\Sigma| \approx 825$ mm, $|\Gamma_F^{\boldsymbol{u}}| \approx 440$ mm, $|\Gamma_F^{\boldsymbol{\sigma}}| \approx 24$ mm. The outer boundary of the fluid space is assumed impermeable except for orange and red segments that form the traction boundary $\Gamma_F^{\boldsymbol{\sigma}}$. (For interpretation of the colors in the figure(s), the reader is referred to the web version of this article.)

$\mu^{-1}(-\Delta_{\Sigma} + I_{\Sigma})^{-1/2}$, cf. Section 4.4. Note that, while $\Sigma$ is now a closed surface, the fractional operator is well defined (and invertible) since the spectrum of the eigenvalue problem (4.5) is positive due to the $H^1$-inner product used in the definition.

The number of iterations required for convergence is tabulated in Table 4.3. With both geometries the iterations are bounded in mesh size. While the axial geometry yields approximately twice as large interface (in terms of the number of degrees of freedom on the interface, $|S_h|$ in Table 4.3), the iteration counts are fairly similar. Moreover, even though the interface is more complex and the interface problem much larger, the number of iterations is in fact comparable to that in the simple setup of Example 2.1 and Section 4.3. We note that the fractional preconditioner leads to convergence in fewer iterations of the MinRes solver especially compared to the simple block-diagonal preconditioner $\mathcal{R}_D$, see Example 2.1. However, the lower setup cost of preconditioner $\mathcal{R}_C$ results in faster solution time (compared to $\mathcal{R}$) despite the increased number of Krylov iterations, see Table 4.4 and Section 4.7 for more detailed discussion.

The resulting Stokes velocity, displacement, and Biot–Stokes fluid pressure fields for the two sets of simulations are shown in Fig. 4.8. Regarding the transverse slices (top panels), the excess pore pressure that develops in the parenchyma drains through the whole interface. However, for the flow and loading rate regime under consideration, the localization of Stokes fluid pressure and the arrows of Stokes velocity (determined by boundary conditions on $\Gamma_{1,F}^{\boldsymbol{\sigma}}$) yield interfacial flow patterns where the pore pressure has a much higher gradient near the bottom-left region of larger velocity. The Biot fluid pressure then dissipates towards the remainder of the deformable porous domain and the permeating patterns seem to match the directions of brain displacement (arrows in the parenchyma region, on the top-right panel). As the flow eventually reaches the interface near the boundary $\Gamma_{2,F}^{\boldsymbol{\sigma}}$, the displacement arrows provide an indication of the direction of interface deformation (which is very small compared to the displacement near the center of the parenchyma. In this case, and for sake of visualization, we portray magnified arrows). In the coronal slices (bottom panels) we can observe that both fluid pressure distributions on the subarachnoid space and brain parenchyma exhibit a higher gradient near the portion of the interface that is closer to $\Gamma_F^{\boldsymbol{\sigma}}$. The bottom-right panel shows a very smooth displacement field with of relatively higher (but still very mild) magnitude near the bottom-center part of the interface. In average, the fluid pressure in the subarachnoid space remains higher than that on the parenchyma. We remark that, as the application here is in 2$d$, we are careful not to draw any conclusion regarding the phenomena in 3$d$. However, our methodology constitutes a promising starting point for accurate and robust algorithms in patient–specific geometries.

### 4.7. Cost comparison of preconditioners

We have demonstrated parameter robustness (cf. Section 4.3) and efficiency of the Biot-Stokes preconditioner (3.12) in terms of reduced number of Krylov iterations relative to other approaches (cf. Table 4.3). However, realization of $\mathcal{R}$ requires inverses of the $2 \times 2$ displacement-velocity block $A$ in (2.13) and the $2 \times 2$ Biot pressure-total pressure block (4.2) which includes the fractional Laplacian (4.3). Due to these components, the exact preconditioner $\mathcal{R}$ might be more costly than the simpler preconditioners $\mathcal{R}_D$ or $\mathcal{R}_C$.

To address the cost efficiency we compare the CPU cost of the preconditioners using the coronal slice geometry (since the problem size $|\mathbf{H}_{\epsilon,h}|$ is then typically larger than with the axial slice). In Table 4.4 we list the setup time of preconditioners $\mathcal{R}$ from (3.12), $\mathcal{R}_D$ from (2.14) and $\mathcal{R}_C$ from (2.15) as well as the timings of the respective preconditioned MinRes solvers together with their cost per iteration. Furthermore, we consider both the exact preconditioners, with the blocks realized by LU decomposition (using the MUMPS library [72]), and approximate preconditioners, where the action of each block is
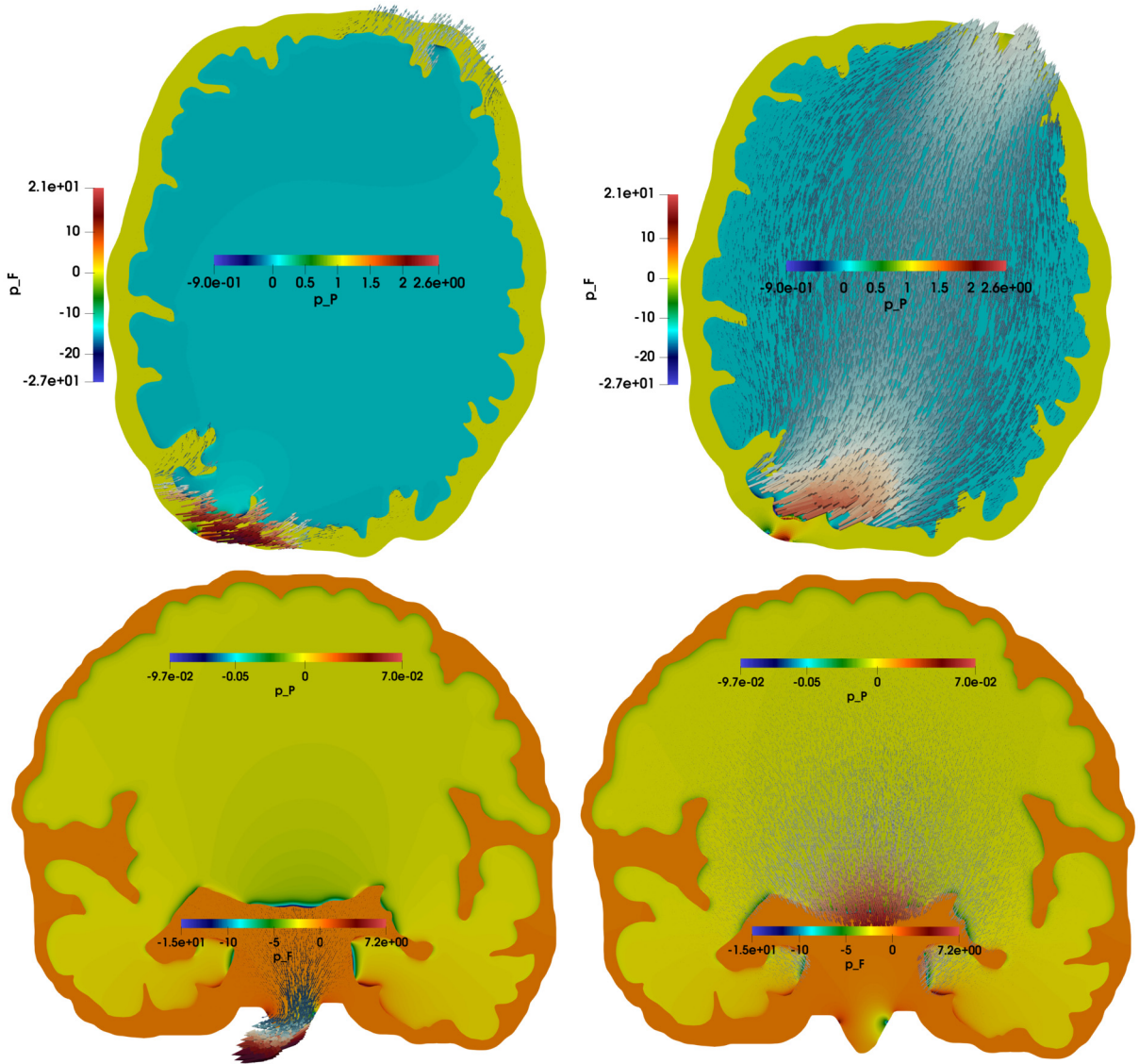
**Fig. 4.8.** Interfacial flow in an idealized geometry. The traction boundary conditions in the top right and bottom left corners (axial slices), respectively at the bottom (coronal slices), induce the fluid flow (left) and the brain displacement (right). The simulations display fluid and displacement fields of localized pressure gradients arising in the cerebrospinal fluid.

computed by single $V$-cycle of algebraic multigrid BoomerAMG[11] from Hypre [73]. In all cases the timings were obtained on Ubuntu workstation with AMD Ryzen Threadripper 3970X 32-Core processor and 128GB of memory. The solvers were run in serial without MPI parallelism.

Using the exact preconditioners we observe that the setup time of $\mathcal{R}_C$ is up to four times shorter compared to $\mathcal{R}$ and the difference translates to fastest overall solution time despite the larger number of MinRes iterations (121 vs. 85 on the finest mesh). We remark that in $\mathcal{R}_C$ the pressure preconditioner is block diagonal (cf. the $2 \times 2$ operator in $\mathcal{R}$) and the operator does not include the fractional Laplacian. However, both preconditioners require inverse of the $2 \times 2$ displacement-velocity block. The difference in setup times then points to the $2 \times 2$ pressure preconditioner (4.2) as the most expensive component of $\mathcal{R}$. Here the large cost is due to assembly of the fractional operator (4.3) and the subsequent inverse of (4.2) which includes a dense block due (4.3). Comparing $\mathcal{R}_C$ and $\mathcal{R}_D$ we note that the additional inverse of $A$ in (2.13) does not seem to introduce significant overhead in setup relative to the fully diagonal preconditioner $\mathcal{R}_D$. Finally, we remark that in this test example the setup and overall solution times of all the preconditioners scale approximately linearly.

---

[11] Parameters of the AMG algorithm were identical for each block, specifically, we used the default parameter values.

**Table 4.4**

Cost comparison of Biot-Stokes preconditioners $\mathcal{R}$ in (3.12), $\mathcal{R}_D$ in (2.14) and $\mathcal{R}_C$ in (2.15). Material parameters from Section 4.6 and meshes based on the coronal brain geometry from Fig. 4.7 are used. Discretization by $TH_1$ elements. (Top) Exact preconditioners inverted by LU and (bottom) approximated by algebraic multigrid are considered. The numbers for each preconditioner show respectively the setup time of the preconditioner, time spent in the MinRes iteration loop, the number of iterations required for convergence and time per iteration (listed in the square brackets). The timings are given in seconds. MinRes solvers are started from random initial guess and converge once reducing the preconditioned residual norm by factor $10^8$. No convergence in 750 iterations is indicated by ——.

| $|H_{\epsilon,h}|$ | $\mathcal{R}$(LU) | | | $\mathcal{R}_D$(LU) | | | $\mathcal{R}_C$(LU) | | |
|---|---|---|---|---|---|---|---|---|---|
| 11681 | 0.6 | 0.4 | 80[0.01] | 0.4 | 1.9 | 406[0.00] | 0.4 | 0.5 | 106[0.01] |
| 36677 | 1.7 | 2.4 | 85[0.03] | 1.0 | 11.3 | 435[0.03] | 1.1 | 3.3 | 116[0.03] |
| 132775 | 6.9 | 8.9 | 88[0.10] | 3.2 | 43.9 | 446[0.10] | 3.6 | 12.5 | 121[0.10] |
| 496680 | 35.7 | 34.7 | 86[0.40] | 11.2 | 163.3 | 440[0.37] | 12.6 | 49.2 | 124[0.40] |
| 1895459 | 159.6 | 126.5 | 85[1.49] | 42.2 | 564.9 | 435[1.30] | 47.6 | 174.3 | 121[1.44] |
| $|\mathbf{H}_{\epsilon,h}|$ | $\mathcal{R}$(AMG) | | | $\mathcal{R}_D$(AMG) | | | $\mathcal{R}_C$(AMG) | | |
| 11681 | 0.5 | 1.2 | 182[0.01] | 0.4 | 2.0 | 392[0.01] | 0.4 | 1.5 | 244[0.01] |
| 36677 | 1.4 | 11.0 | 293[0.04] | 0.9 | 14.3 | 507[0.03] | 1.0 | 14.5 | 410[0.04] |
| 132775 | 5.4 | 83.1 | 533[0.16] | 2.7 | 92.7 | ——[0.12] | 2.8 | 107.5 | ——[0.14] |
| 496680 | 24.6 | 453.6 | ——[0.60] | 9.1 | 363.4 | ——[0.48] | 9.4 | 401.7 | ——[0.54] |
| 1895459 | 99.3 | 1804.2 | ——[2.41] | 33.4 | 1575.6 | ——[2.10] | 35.8 | 1606.8 | ——[2.14] |

For scalability of $\mathcal{R}$ in $3d$ problems, the preconditioner blocks need to be computed by more efficient methods than LU. To this end, tailored algorithms are required. We illustrate this need in Table 4.4 where the preconditioners are realized by algebraic multigrid. It can be seen that, while the setup times have been reduced, the chosen multigrid provides poor approximation of the inverse, resulting in slow convergence of the Krylov solvers.

The lack of convergence with both $\mathcal{R}$ and $\mathcal{R}_C$ suggests that specialized solvers/improved AMG are required both for the displacement-velocity block $A$ in (2.13), which includes the metric term on the interface due to the tangential coupling, and the pressure block (4.2). To the best of the authors' efficient methods for these two components are currently missing in general. However, auxiliary multigrid developed in [74] could be applicable in approximating the first block $A$ of (3.12) and (2.15). Moreover, numerous scalable algorithms exist for the fractional Laplacian, e.g., quadrature methods [75], rational approximations [76,77] or multilevel methods [78–80]. These algorithms could serve as building blocks in solvers for (4.2).

## 5. Conclusions

In this paper, we considered discretizations of a multiphysics model describing interaction between the free flow of a viscous Newtonian fluid and a deformable porous medium separated by an interface. The problem was formulated in terms of Stokes velocity-pressure and Biot displacement-total pressure-fluid pressure; no additional variables were introduced on the interface to account for the coupling. The investigations carried out here have been motivated by both theoretical numerical analysis and computational experiments. The well-posedness of the resulting five-field formulation was established using appropriately weighted operators in fractional Sobolev and metric spaces at the interface resulting in stability in all material parameters. In turn, parameter robust block-diagonal preconditioners were proposed for the underlying saddle-point linear system. On the other hand, parameter robustness of the exact preconditioner was demonstrated through several test cases using conforming and non-conforming finite element discretizations. Efficiency of the preconditioner was assessed on an application to interfacial flow in the brain with realistic two-dimensional geometries. Our results have demonstrated that, in scaling the preconditioner to large scale (three-dimensional) problems, black-box algorithms might not be sufficient. In this regard, the construction of tailored efficient solvers for the components of the proposed preconditioner constitutes a very much needed avenue for future research.

We emphasize that the methods and analysis put forward in this work can be readily generalized to address more complex boundary and interfacial conditions, spatially heterogeneous material parameters, anisotropy, including gravity and osmotic pressure effects, other types of stable discretizations, and other parameter regimes observed in brain poromechanics, such as traumatic brain injury, treatment of hematoma development, blocking of aqueducts in hydrocephalus, and magnetic resonance elastography where the brain tissue is loaded under small strains at high frequencies. However further effort is needed in validating the current results against clinical data.

## CRediT authorship contribution statement

**Wietse M. Boon:** Conceptualization, Formal analysis, Writing – original draft, Writing – review & editing. **Martin Hornkjøl:** Formal analysis, Investigation, Writing – original draft, Writing – review & editing. **Miroslav Kuchta:** Formal analysis, Investigation, Methodology, Software, Visualization, Writing – original draft, Writing – review & editing. **Kent-André Mardal:** Conceptualization, Formal analysis, Investigation, Methodology, Writing – original draft, Writing – review & editing. **Ricardo Ruiz-Baier:** Conceptualization, Formal analysis, Methodology, Writing – original draft, Writing – review & editing.

**Declaration of competing interest**

The authors declare that they have no known competing financial interests or personal relationships that could have appeared to influence the work reported in this paper.

## Appendix A. TH$_k$ and CR finite element families

We denote by $\{\mathcal{T}_h\}_{h>0}$ a shape-regular family of partitions of $\bar{\Omega}$, conformed by tetrahedra (or triangles in 2D) $K$ of diameter $h_K$, with mesh size $h := \max\{h_K : K \in \mathcal{T}_h\}$, and denote $\mathcal{T}_h^F$ and $\mathcal{T}_h^P$ the restrictions of the mesh elements to the subdomains $\Omega_F$ and $\Omega_P$, respectively. Similarly, by $\mathcal{E}_h^F$ and $\mathcal{E}_h^P$ we will denote the restrictions to the interior mesh facets (edges in 2D) to the Stokes and Biot subdomains, respectively. We assume that the two partitions match at the interface. Given an integer $k \geq 1$ and a subset $S$ of $\mathbb{R}^d$, $d = 2, 3$, by $\mathbb{P}_k(S)$ we will denote the space of polynomial functions defined locally in $S$ and being of total degree up to $k$. The methods that we use are based on the generalized Taylor–Hood [46] and Crouzeix–Raviart [47] finite element families that give an overall $k+1$ order of convergence. Their definition is recalled next

$$
\text{TH}_k \begin{cases}
\vec{V}_h = \{(\boldsymbol{v}_h, \boldsymbol{w}_h) \in \vec{V} : \boldsymbol{v}_h|_K \in \mathbb{P}_{k+1}(K)^d, \boldsymbol{w}_h|_L \in \mathbb{P}_{k+1}(L)^d, \forall K \in \mathcal{T}_h^F, L \in \mathcal{T}_h^P\}, \\
\vec{Q}_h = \{\vec{q}_h \in \vec{Q} \cap [C(\Omega_F) \times C(\Omega_P) \times L^2(\Omega_P)] : \\
\qquad q_{F,h}|_K \in \mathbb{P}_k(K), \psi_h|_L \in \mathbb{P}_k(L), q_{P,h}|_L \in \mathbb{P}_{k+1}(L), \forall K \in \mathcal{T}_h^F, L \in \mathcal{T}_h^P\},
\end{cases}
$$

$$
\text{CR} \begin{cases}
\vec{V}_h = \{(\boldsymbol{v}_h, \boldsymbol{w}_h) \in \mathbf{L}^2(\Omega_F) \times \mathbf{L}^2(\Omega_P) : \boldsymbol{v}_h|_K \in \mathbb{P}_1(K)^d, \boldsymbol{w}_h|_L \in \mathbb{P}_1(L)^d, \\
\qquad \int_e [\![ T_{\boldsymbol{n}_e} \boldsymbol{v}_h ]\!] = 0, \int_\ell [\![ T_{\boldsymbol{n}_\ell} \boldsymbol{w}_h ]\!] = 0, \quad \forall e \subset \partial K, \ell \subset \partial L, \ K \in \mathcal{T}_h^F, L \in \mathcal{T}_h^P\}, \\
\vec{Q}_h = \{\vec{q}_h \in \vec{Q} \cap [L^2(\Omega_F) \times L^2(\Omega_P) \times C(\Omega_P)] : q_{F,h}|_K \in \mathbb{P}_0(K), \\
\qquad \psi_h|_L \in \mathbb{P}_0(L), q_{P,h}|_L \in \mathbb{P}_1(L), \quad \forall K \in \mathcal{T}_h^F, L \in \mathcal{T}_h^P\}.
\end{cases}
$$

## Appendix B. CR discretization for the Biot system

Due to the chosen facet stabilization required by the CR family, the discretization of the velocity-displacement operator $A$ defined in (2.13) includes addition terms. More specifically, we consider

$$
\langle A_h(\boldsymbol{u}, \boldsymbol{d}), (\boldsymbol{v}, \boldsymbol{w}) \rangle = \int_{\Omega_F} 2\mu_f \boldsymbol{\epsilon}(\boldsymbol{u}) : \boldsymbol{\epsilon}(\boldsymbol{v}) + \sum_{e \in \mathcal{E}_h^F} \int_e \frac{2\mu_f}{|e|} [\![ T_{\boldsymbol{n}} \boldsymbol{u} ]\!] [\![ T_{\boldsymbol{n}} \boldsymbol{v} ]\!]
$$

$$
+ \int_{\Omega_P} 2\mu_s \boldsymbol{\epsilon}(\boldsymbol{d}) : \boldsymbol{\epsilon}(\boldsymbol{w}) + \sum_{e \in \mathcal{E}_h^P} \int_e \frac{2\mu_s}{|e|} [\![ T_{\boldsymbol{n}} \boldsymbol{d} ]\!] [\![ T_{\boldsymbol{n}} \boldsymbol{w} ]\!]
$$

$$
+ \frac{\gamma \mu_f}{\sqrt{\kappa}} \int_\Sigma T_{\boldsymbol{t}}(\boldsymbol{u} - \boldsymbol{d}) \cdot T_{\boldsymbol{t}}(\boldsymbol{v} - \boldsymbol{w}),
$$

for all $(\boldsymbol{u}, \boldsymbol{d}), (\boldsymbol{v}, \boldsymbol{w}) \in \vec{V}_h$, while the remaining components $B$, $C$ of the Biot-Stokes operator remain unchanged. We remark that the discrete operator $A_h$ is also used in the discretization of preconditioner $\mathcal{R}$ in (3.12).

We investigate numerically the stability of the three-field (total pressure) formulation of Biot equations discretized by the CR family. Assuming momentarily that $\partial\Omega_P = \Gamma_P^{\boldsymbol{d}}$ the discrete weak problem reads: Find $(\boldsymbol{d}_h, p_{P,h}, \varphi_h) \in \mathbf{W}_h \times Q_h^P \times Z_h$ such that for all $(\boldsymbol{w}_h, q_{P,h}, Z_h) \in \mathbf{W}_h \times Q_h^P \times Z_h$ it holds that

$$
\int_{\Omega_P} 2\mu_s \boldsymbol{\epsilon}(\boldsymbol{d}_h) : \boldsymbol{\epsilon}(\boldsymbol{w}_h) + \sum_{e \in \mathcal{E}_h^P} \int_e \frac{2\mu_f}{|e|} [\![ T_{\boldsymbol{n}} \boldsymbol{d}_h ]\!] [\![ T_{\boldsymbol{n}} \boldsymbol{w}_h ]\!] - \int_{\Omega_P} \varphi_h \operatorname{div} \boldsymbol{w}_h = \int_{\Omega_P} \boldsymbol{f} \cdot \boldsymbol{w}_h,
$$

$$
- \int_{\Omega_P} \frac{\alpha^2}{\lambda} p_{P,h} q_{P,h} - \int_{\Omega_P} \frac{\kappa}{\mu_f} \nabla p_{P,h} \cdot \nabla q_{P,h} + \int_{\Omega_P} \frac{\alpha}{\lambda} \varphi_h q_{P,h} = 0, \tag{B.1}
$$

$$
\int_{\Omega_P} \psi_h \left( -\operatorname{div} \boldsymbol{d}_h + \frac{\alpha}{\lambda} p_{P,h} - \frac{1}{\lambda} \varphi_h \right) = 0.
$$

In Fig. B.1 we report the number of iterations required for convergence of MinRes solver started from random initial vector until reducing the preconditioned residual norm by a factor of $10^8$. Here the preconditioner analyzed in [27] (that is, the preconditioner is formed by the second, fourth and final blocks of the operator $\mathcal{R}_D$ in (2.14)) is used. We remark that
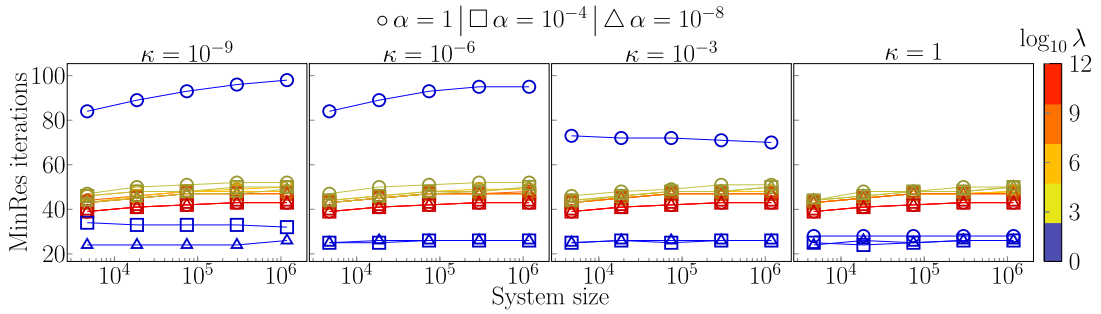
**Fig. B.1.** Total pressure Biot formulation (B.1) with preconditioner from [27], and using a discretization by CR family.
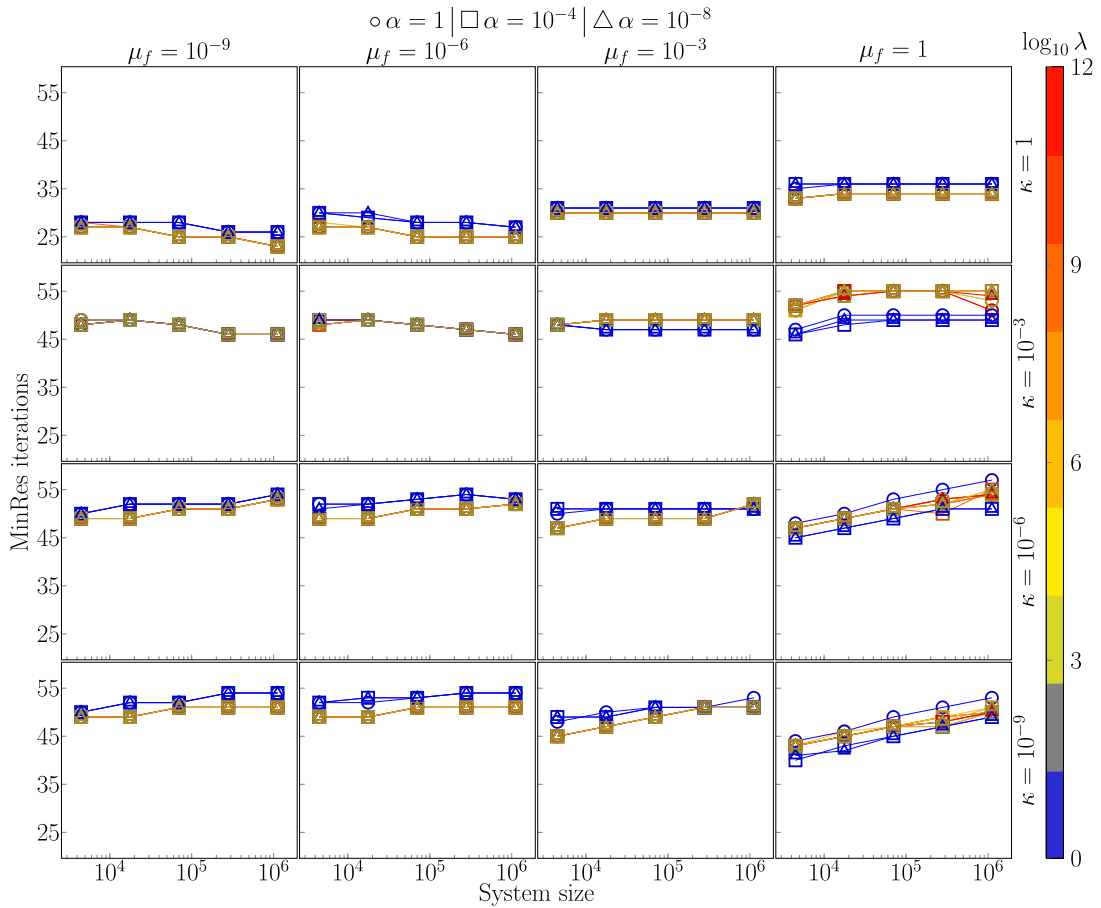


**Fig. B.2.** Performance of Biot–Stokes preconditioner (3.12). Geometry of Example 2.1 is used with $\Sigma$ intersecting $\Gamma_F^\sigma$ and $\Gamma_P^{p_p}$. The fractional operator is changed to $\mu^{-1}(-\Delta_\Sigma + I_\Sigma)^{-1/2}$. We set $\mu_s = 1$, $C_0 = 0$, $\gamma = 10^2$. The parameters $\mu_f$, $\kappa$, $\lambda$, $\alpha$ are varied. Values of the Biot-Willis coefficient are indicated by markers. The discretization is done using the CR family.

in the numerical experiment $\Omega_P = (0, 1)^2$, and $|\Gamma_P^{p_p}| \cdot |\Gamma_P^{\boldsymbol{d}}| > 0$. We observe that the iterations are bounded with respect to the mesh size as well as to variations in material parameters.

## References

[1] M.A. Murad, J.N. Guerreiro, A.F. Loula, Micromechanical computational modeling of secondary consolidation and hereditary creep in soils, Comput. Methods Appl. Mech. Eng. 190 (15) (2001) 1985–2016.

[2] R.E. Showalter, Poroelastic filtration coupled to Stokes flow, in: O. Imanuvilov, G. Leugering, R. Triggiani, B.-Y. Zhang (Eds.), Control Theory of Partial Differential Equations, in: Lecture Notes in Pure and Applied Mathematics, vol. 242, Chapman & Hall, Boca Raton, 2005, pp. 229–241.

[3] E.A. Bergkamp, C.V. Verhoosel, J.J.C. Remmers, D.M.J. Smeulders, A staggered finite element procedure for the coupled Stokes-Biot system with fluid entry resistance, Comput. Geosci. 24 (2020) 1497–1522.

[4] C. Ager, B. Schott, M. Winter, W.A. Wall, A Nitsche-based cut finite element method for the coupling of incompressible fluid flow with poroelasticity, Comput. Methods Appl. Mech. Eng. 351 (2019) 253–280.

[5] I. Ambartsumyan, E. Khattatov, I. Yotov, P. Zunino, A Lagrange multiplier method for a Stokes–Biot fluid–poroelastic structure interaction model, Numer. Math. 140 (2) (2018) 513–553, https://doi.org/10.1007/s00211-018-0967-1.

[6] S. Badia, A. Quaini, A. Quarteroni, Coupling Biot and Navier-Stokes equations for modelling fluid-poroelastic media interaction, J. Comput. Phys. 228 (2009) 7986–8014.

[7] M. Bukač, I. Yotov, R. Zakerzadeh, P. Zunino, Partitioning strategies for the interaction of a fluid with a poroelastic material based on a Nitsche's coupling approach, Comput. Methods Appl. Mech. Eng. 292 (2015) 138–170.

[8] S. Caucao, T. Li, I. Yotov, A multipoint stress-flux mixed finite element method for the Stokes-Biot model, preprint, arXiv:2011.01396, 2020.

[9] A. Cesmelioglu, Analysis of the coupled Navier-Stokes/Biot problem, J. Math. Anal. Appl. 456 (2) (2017) 970–991.

[10] A. Cesmelioglu, P. Chidyagwai, Numerical analysis of the coupling of free fluid with a poroelastic material, Numer. Methods Partial Differ. Equ. 36 (3) (2020) 463–494.

[11] T. Li, I. Yotov, A mixed elasticity formulation for fluid-poroelastic structure interaction, preprint, arXiv:2011.00132, 2020.

[12] M. Taffetani, R. Ruiz-Baier, S.L. Waters, Coupling Stokes flow with inhomogeneous poroelasticity, Q. J. Mech. Appl. Math. 74 (4) (2021) 411–439, https://doi.org/10.1093/qjmam/hbab014.

[13] J. Wen, Y. He, A strongly conservative finite element method for the coupled Stokes-Biot model, Comput. Math. Appl. 80 (2020) 1421–1442, https://doi.org/10.1016/j.camwa.2020.07.001.

[14] J. Wen, J. Su, Y. He, H. Chen, Discontinuous Galerkin method for the coupled Stokes-Biot model, Numer. Methods Partial Differ. Equ. 37 (2021) 383–405, https://doi.org/10.1002/num.22532.

[15] H.K. Wilfrid, Nonconforming finite element methods for a Stokes/Biot fluid–poroelastic structure interaction model, Results Appl. Math. 7 (2020) 100127, https://doi.org/10.1016/j.rinam.2020.100127.

[16] R. Ruiz-Baier, M. Taffetani, H.D. Westermeyer, I. Yotov, The Biot-Stokes coupling using total pressure: formulation, analysis and application to interfacial flow in the eye, Comput. Methods Appl. Mech. Eng. 389 (2022) e114384, https://doi.org/10.1016/j.cma.2021.114384, 1–30.

[17] I. Ambartsumyan, V.J. Ervin, T. Nguyen, I. Yotov, A nonlinear Stokes-Biot model for the interaction of a non-Newtonian fluid with poroelastic media, ESAIM: Math. Model. Numer. Anal. 53 (6) (2019) 1915–1955.

[18] R. Bürger, S. Kumar, D. Mora, R. Ruiz-Baier, N. Verma, Virtual element methods for the three-field formulation of time-dependent linear poroelasticity, Adv. Comput. Math. 47 (2021) e2, 1–37.

[19] S. Kumar, R. Oyarzúa, R. Ruiz-Baier, R. Sandilya, Conservative discontinuous finite volume and mixed schemes for a new four-field formulation in poroelasticity, ESAIM: Math. Model. Numer. Anal. 54 (1) (2020) 273–299.

[20] R. Oyarzúa, R. Ruiz-Baier, Locking-free finite element methods for poroelasticity, SIAM J. Numer. Anal. 54 (5) (2016) 2951–2973.

[21] W.M. Boon, T. Koch, M. Kuchta, K.-A. Mardal, Robust monolithic solvers for the Stokes-Darcy problem with the Darcy equation in primal form, preprint, arXiv:2110.07486, 2021.

[22] P. Chidyagwai, S. Ladenheim, D.B. Szyld, Constraint preconditioning for the coupled Stokes–Darcy system, SIAM J. Sci. Comput. 38 (2) (2016) A668–A690.

[23] K.E. Holter, M. Kuchta, K.-A. Mardal, Robust preconditioning for coupled Stokes–Darcy problems with the Darcy problem in primal form, Comput. Math. Appl. 91 (2021) 56–66.

[24] T. Karper, K.-A. Mardal, R. Winther, Unified finite element discretizations of coupled Darcy–Stokes flow, Numer. Methods Partial Differ. Equ. 25 (2) (2009) 311–326.

[25] K.-A. Mardal, R. Winther, Preconditioning discretizations of systems of partial differential equations, Numer. Linear Algebra Appl. 18 (2011) 1–40.

[26] K.-A. Mardal, M.E. Rognes, T.B. Thompson, Accurate discretization of poroelasticity without Darcy stability, BIT Numer. Math. (2021) 1–36.

[27] J. Lee, K.-A. Mardal, R. Winther, Parameter-robust discretization and preconditioning of Biot's consolidation model, SIAM J. Sci. Comput. 39 (1) (2017) A1–A24.

[28] J. Lee, E. Piersanti, K.-A. Mardal, M. Rognes, A mixed finite element method for nearly incompressible multiple-network poroelasticity, SIAM J. Sci. Comput. 41 (2) (2019) A722–A747.

[29] W. Boon, M. Kuchta, K.-A. Mardal, R. Ruiz-Baier, Robust preconditioners and stability analysis for perturbed saddle-point problems – application to conservative discretizations of Biot's equations utilizing total pressure, SIAM J. Sci. Comput. 43 (4) (2021) B961–B983.

[30] T. Bærland, M. Kuchta, K.-A. Mardal, T. Thompson, An observation on the uniform preconditioners for the mixed Darcy problem, Numer. Methods Partial Differ. Equ. (2020) 1–17.

[31] J. Bergh, J. Löfström, Interpolation Spaces: An Introduction, vol. 223, Springer Science & Business Media, 2012.

[32] G.N. Gatica, A Simple Introduction to the Mixed Finite Element Method, Springer-Verlag, Berlin, 2014.

[33] C. le Roux, B.D. Reddy, The steady Navier-Stokes equations with mixed boundary conditions: application to free boundary flows, Nonlinear Anal., Theory Methods Appl. 20 (9) (1993) 1043–1068, https://doi.org/10.1016/0362-546X(93)90094-9.

[34] J. Pestana, A.J. Wathen, Natural preconditioning and iterative methods for saddle point systems, SIAM Rev. 57 (1) (2015) 71–91.

[35] T.A. Driscoll, K.-C. Toh, L.N. Trefethen, From potential theory to matrix iterations in six steps, SIAM Rev. 40 (3) (1998) 547–578.

[36] T. Rusten, R. Winther, A preconditioned iterative method for saddlepoint problems, SIAM J. Matrix Anal. Appl. 13 (3) (1992) 887–904.

[37] D. Silvester, A. Wathen, Fast iterative solution of stabilised stokes systems part ii: using general block preconditioners, SIAM J. Numer. Anal. 31 (5) (1994) 1352–1367.

[38] J. Liesen, P. Tichý, Convergence analysis of Krylov subspace methods, GAMM-Mitt. 27 (2) (2004) 153–173.

[39] D. Braess, Stability of saddle point problems with penalty, ESAIM: Math. Model. Numer. Anal. 30 (6) (1996) 731–742.

[40] V. Girault, P.-A. Raviart, Finite Element Methods for Navier-Stokes Equations: Theory and Algorithms, 1st edition, Springer Publishing Company, 1986.

[41] A. Ern, J.-L. Guermond, Theory and Practice of Finite Elements, Appl. Math. Sci., vol. 159, Springer-Verlag, New York, 2004.

[42] V. Anaya, A. Khan, D. Mora, R. Ruiz-Baier, Robust a posteriori error analysis for rotation-based formulations of the elasticity/poroelasticity coupling, SIAM J. Sci. Comput. (2022).

[43] J. Galvis, M. Sarkis, Non-matching mortar discretization analysis for the coupling Stokes-Darcy equations, Electron. Trans. Numer. Anal. 26 (2007) 350–384.

[44] W.J. Layton, F. Schieweck, I. Yotov, Coupling fluid flow with porous media flow, SIAM J. Numer. Anal. 40 (6) (2002) 2195–2218.

[45] M. Arioli, D. Loghin, Discrete interpolation norms with applications, SIAM J. Numer. Anal. 47 (4) (2009) 2924–2951.

[46] D. Boffi, Stability of higher order triangular Hood-Taylor methods for the stationary Stokes equations, Math. Models Methods Appl. Sci. 4 (02) (1994) 223–235.

[47] M. Crouzeix, P.-A. Raviart, Conforming and nonconforming finite element methods for solving the stationary Stokes equations I, ESAIM: Math. Model. Numer. Anal. 7 (R3) (1973) 33–75.

[48] B.P. Lamichhane, A new stabilization technique for the nonconforming Crouzeix–Raviart element applied to linear elasticity, Appl. Math. Lett. 39 (2015) 35–41, https://doi.org/10.1016/j.aml.2014.08.005.

[49] E. Burman, P. Hansbo, Stabilized Crouzeix-Raviart element for the Darcy-Stokes problem, Numer. Methods Partial Differ. Equ. 21 (5) (2005) 986–997, https://doi.org/10.1002/num.20076.

[50] D. Boffi, F. Brezzi, M. Fortin, Mixed Finite Element Methods and Applications, vol. 44, Springer-Verlag, Berlin, 2013.

[51] M.S. Alnæs, J. Blechta, J. Hake, A. Johansson, B. Kehlet, A. Logg, C. Richardson, J. Ring, M.E. Rognes, G.N. Wells, The FEniCS project version 1.5, Arch. Numer. Softw. 3 (100) (2015) 9–23.

[52] A. Logg, K.-A. Mardal, G. Wells, Automated Solution of Differential Equations by the Finite Element Method, Springer-Verlag, Berlin, Germany, 2012.

[53] M. Kuchta, Assembly of multiscale linear PDE operators, in: F.J. Vermolen, C. Vuik (Eds.), Numerical Mathematics and Advanced Applications, ENUMATH 2019, Springer International Publishing, Cham, 2021, pp. 641–650.

[54] M. Kuchta, M. Nordaas, J. Verschaeve, M. Mortensen, K. Mardal, Preconditioners for saddle point systems with trace constraints coupling 2D and 1D domains, SIAM J. Sci. Comput. 38 (6) (2016) B962–B987.

[55] E. Burman, Projection stabilization of Lagrange multipliers for the imposition of constraints on interfaces and boundaries, Numer. Methods Partial Differ. Equ. 30 (2) (2014) 567–592.

[56] B.I. Wohlmuth, A mortar finite element method using dual spaces for the Lagrange multiplier, SIAM J. Numer. Anal. 38 (3) (2000) 989–1012.

[57] J.C.C. Nitsche, Über ein variationsprinzip zur lösung von Dirichlet-problemen bei verwendung von teilräumen, die keinen randbedingungen unterworfen sind, Abh. Math. Semin. Univ. Hamb. 36 (1971) 9–15.

[58] J. Droniou, N. Nataraj, Improved $L^2$ estimate for gradient schemes and super-convergence of the TPFA finite volume scheme, IMA J. Numer. Anal. 38 (3) (2017) 1254–1293, https://doi.org/10.1093/imanum/drx028.

[59] K.H. Støverud, M. Alnæs, H.P. Langtangen, V. Haughton, K.-A. Mardal, Poro-elastic modeling of Syringomyelia—a systematic study of the effects of pia mater, central canal, median fissure, white and gray matter on pressure wave propagation and fluid movement within the cervical spinal cord, Comput. Methods Biomech. Biomed. Eng. 19 (6) (2016) 686–698.

[60] B. Tully, Y. Ventikos, Cerebral water transport using multiple-network poroelastic theory: application to normal pressure hydrocephalus, J. Fluid Mech. 667 (2011) 188–215.

[61] K.E. Holter, B. Kehlet, A. Devor, T.J. Sejnowski, A.M. Dale, S.W. Omholt, O.P. Ottersen, E.A. Nagelhus, K.-A. Mardal, K.H. Pettersen, Interstitial solute transport in 3d reconstructed neuropil occurs by diffusion rather than bulk flow, Proc. Natl. Acad. Sci. 114 (37) (2017) 9894–9899.

[62] R. Kedarasetti, P.J. Drew, F. Costanzo, Arterial vasodilation drives convective fluid flow in the brain: a poroelastic model, bioRxiv, 2021.

[63] J. Tithof, K.A. Boster, P.A. Bork, M. Nedergaard, J.H. Thomas, D.H. Kelley, a network model of glymphatic flow under different experimentally-motivated parametric scenarios, bioRxiv, 2021.

[64] S. Budday, R. Nay, R. de Rooij, P. Steinmann, T. Wyrobek, T.C. Ovaert, E. Kuhl, Mechanical properties of gray and white matter brain tissue by indentation, J. Mech. Behav. Biomed. Mater. 46 (2015) 318–330.

[65] J.H. Smith, J.A. Humphrey, Interstitial transport and transvascular fluid exchange during infusion into brain and tumor tissue, Microvasc. Res. 73 (1) (2007) 58–73.

[66] A. Klawonn, Block-triangular preconditioners for saddle point problems with a penalty term, SIAM J. Sci. Comput. 19 (1) (1998) 172–184.

[67] B.S. Southworth, S.A. Olivier, A note on $2 \times 2$ block-diagonal preconditioning, preprint, arXiv:2001.00711, 2020.

[68] B. Fischer, A. Ramage, D.J. Silvester, A.J. Wathen, Minimum residual methods for augmented systems, BIT Numer. Math. 38 (3) (1998) 527–543.

[69] N.A. Jessen, A.S.F. Munk, I. Lundgaard, M. Nedergaard, The glymphatic system: a beginner's guide, Neurochem. Res. 40 (12) (2015) 2583–2599.

[70] R.T. Kedarasetti, K.L. Turner, C. Echagarruga, B.J. Gluckman, P.J. Drew, F. Costanzo, Functional hyperemia drives fluid exchange in the paravascular space, Fluids Barriers CNS 17 (1) (2020) 1–25.

[71] C. Daversin-Catty, V. Vinje, K.-A. Mardal, M.E. Rognes, The mechanisms behind perivascular fluid flow, PLoS ONE 15 (12) (2020) e0244442.

[72] P. Amestoy, I.S. Duff, J. Koster, J.-Y. L'Excellent, A fully asynchronous multifrontal solver using distributed dynamic scheduling, SIAM J. Matrix Anal. Appl. 23 (1) (2001) 15–41.

[73] R.D. Falgout, U.M. Yang, hypre: a library of high performance preconditioners, in: P.M.A. Sloot, A.G. Hoekstra, C.J.K. Tan, J.J. Dongarra (Eds.), Computational Science — ICCS 2002, Springer Berlin Heidelberg, Berlin, Heidelberg, 2002, pp. 632–641.

[74] A. Budisa, W.M. Boon, X. Hu, Mixed-dimensional auxiliary space preconditioners, SIAM J. Sci. Comput. 42 (5) (2020) A3367–A3396.

[75] A. Bonito, J.P. Borthagaray, R.H. Nochetto, E. Otárola, A.J. Salgado, Numerical methods for fractional diffusion, Comput. Vis. Sci. 19 (5) (2018) 19–46.

[76] S. Harizanov, R. Lazarov, S. Margenov, P. Marinov, Y. Vutov, Optimal solvers for linear systems with fractional powers of sparse spd matrices, Numer. Linear Algebra Appl. 25 (5) (2018) e2167.

[77] C. Hofreither, An algorithm for best rational approximation based on barycentric rational interpolation, Numer. Algorithms 88 (1) (2021) 365–388.

[78] J. Bramble, J. Pasciak, P. Vassilevski, Computational scales of Sobolev norms with application to preconditioning, Math. Comput. 69 (230) (2000) 463–480.

[79] T. Bærland, M. Kuchta, K.-A. Mardal, Multigrid methods for discrete fractional Sobolev spaces, SIAM J. Sci. Comput. 41 (2) (2019) A948–A972.

[80] T. Führer, Multilevel decompositions and norms for negative order Sobolev spaces, Math. Comput. (2021).